鐵-鋁-鈦和鐵-鋁-錳合金相變化、
機械性質及耐腐蝕研究

研究生：蔡 國 棟　　　　　　　　指導教授：劉 增 豐 博士

朝 春 光 博士

國立交通大學材料科學與工程研究所

中文摘要

本論文利用光學顯微鏡（OM）、穿透式電子顯微鏡（TEM）、X 光能量散佈分析儀（EDS）、X 光繞射儀（XRD）、歐傑電子分析儀（AES）等儀器，研究鐵-24.6 at.%鋁-7.5 at.%鈦三元合金顯微結構的變化，同時探討鐵-20 at.%鋁-26 at.%錳-(5-8) at.%碳合金在淬火狀態下，合金中不同碳素含量對於史賓諾多相分解反應的影響，以及進一步研究在鐵-(7.1-9.1) wt.% 鋁 -(29.2-31.3) wt.% 錳 -(2.8-6) wt.% 鉻 -(0.88-1.07) wt.% 碳 (鐵 -(13.2-16.4) at.%鋁-(26.6-27.8) at.%錳-(2.7-5.6) at.%鉻-(3.7-4.3) at.%碳) 系列合金中，不同的鉻含量對於機械性能及耐蝕性的研究。本論文所得到的具體研究結果如下：

[1]、先前研究顯示，Ti 元素的添加對二元的 Ti-Al 合金將會有（1）大幅提升 $D0_3 \rightarrow B2$ 及 $B2 \rightarrow A2$ 相轉換溫度，（2）顯著擴大$(A2+D0_3)$相區域，及（3）促使 $D0_3$ 反向晶界傾向於非等方性（anisotropy）。此外，Fe-Al-Ti 三元合金於 1073~1273K 時，存在一$(B2+L2_1)$雙相區（此三元合

金中的 $L2_1$，等同在二元合金中的 $D0_3$ 結構），值得注意的是，此$(B2+D0_3)$雙相區於 Fe-Al 二元合金中從未被先前研究者所發現。然而，於 Fe-Al-Ti 三元合金中所存在之$(B2+L2_1)$雙相區，主要亦是藉由 X 光繞射儀（XRD）、熱示差掃描卡量計（DSC）、熱差分析儀（DTA）及電子探針微分析儀（EPMA）。近來我們利用穿透式電子顯微鏡針對鐵-23 at.%鋁-8.5 at.%鈦合金經過 1173K 時效後，進行相變化研究，發現於 1173K 較長時間時效後，$L2_1$ 相區大幅擴大，且於 a/2<100>反向晶界(anti-phase boundary, APB)，依序發生一 $A2 \rightarrow (A2+L2_1) \rightarrow (B2+L2_1)$的相變化，此一現象從未被其他研究者發現。延續先前研究，此次研究目的乃針對鐵-24.6 at.%鋁-7.5 at.%鈦合金經過 1173K 時效後，嘗試觀察顯微組織的發展情形。值得注意的是，依據先前所建立的 Fe-Al-Ti 三元合金等溫相圖，前述合金與本研究合金的化學組成均落入$(B2+L2_1)$相區，然而本研究合金的組成更逼近 A2/ B2/$L2_1$ 相區頂端。

研究結果顯示，在淬火狀態，鐵-23 at.%鋁-7.5 at.%鈦合金為$(A2+L2_1)$混合相，續於 1173K 施予 6 小時時效後，$L2_1$ 相大幅成長，且在 a/2<100>反向晶界上可見 B2 相顆粒存在形成；隨著時效時間延長，$L2_1$ 相的 domain 大幅成長，且在 a/2<100>反向晶界鄰近區 $L2_1$ 相分離(phase separation) 為 $(B2+ L2_1^*)$。其中 $L2_1^*$亦為 $L2_1$ 相。1173K 時效時間繼續延長，相分離朝向整個已成長的 $L2_1$ 相區內部。因而合金於 1173K 施予 36 小時時效後，則呈現 $(B2+ L2_1^*)$ 混合的顯微組織。

[2]、完全沃斯田鐵相 FeAlMnC 合金，其顯微組織已廣泛被諸多學者研究。這些研究顯示，當合金組成在鐵-(7.8–11.8) wt.%鋁-(28–34.3) wt.%錳-(0.74–1.3) wt.%碳（鐵-(14.2–20.9) at.%鋁-(25–30.1) at.%錳-(3.1–5.2) at.%碳）範圍，於單一沃斯田鐵（γ）相（無序面心立方（fcc））區域做固溶化熱處理後急冷，其顯微組織為單一沃斯田鐵相。續於 500–550 °C 做適度時間的時效處理，細緻的(Fe,Mn)$_3$AlC$_x$ 碳化物 (k′碳化物)開始於沃斯田鐵基地中以整合（coherent）析出，此(Fe,Mn)$_3$AlC$_x$ 碳化物具有一種有序的面心立方 L′1$_2$ 型結構。最近我們以穿透式電子顯微鏡觀察一鐵-9 wt.%鋁-30 wt.%錳-2 wt.%碳 （鐵-16 at.%鋁-26 at.%錳-8 at.%碳）合金的相變化。結果發現在淬火狀況下，單一的沃斯田鐵中蘊含有以史賓諾多相分解反應的細緻 k′碳化物存在，此與碳含量介於 3.1≤C≤5.2 at.%的 FeAlMnC 合金中，k′碳化物僅可見於合金經時效處理後迥然不同。這個發現顯示碳含量對淬火時 k′碳化物於沃斯田鐵基地中的形成扮演著重要的角色。然而，迄今，為何添加較多的碳含量會促使有如此結果的理由尚不清楚，因此本研究的主要目的，則在於有系統的分析鐵-20 at.%鋁-26 at.%錳-(5.0-8.0) at%碳合金的淬火顯微組織。

研究結果顯示，在淬火狀態下，於鐵-20 at.%鋁-26 at.%錳-碳合金，碳含量在 5.5≤C≤8.0 at.%時，可見史賓諾多相分解反應與有序的 k′碳化物形成。且隨著碳含量的逐漸增加，史賓諾多的波長和有序的 k′碳化物含量，兩者均遞增，顯然史賓諾多相分解反應及有序化的反應溫度隨碳含

量之增加而增加。隨著碳含量的增加，有序的 k′ 碳化物及無序的 γ_0 相，兩者的晶格常數均增加，然而晶格的 misfit 卻下降，且當碳含量略低於 5.5 at.%時 misfit 卻急遽增加。其顯示碳含量略低於 5.5 at.%時，其 k′ 碳化物和 γ_0 相之間的應變能（strain energy）急遽的增加。由於應變能急遽增加，過冷（undercooling）可能尚不足以克服應變能量的增加，而抑制了史賓諾多相分解和有序 k′ 碳化物在淬火過程中形成。其說明本研究中的合金 A (5 C)和先前 3.1≤C≤5.2 at.%沃斯田鐵系 FeAlMnC 合金，於淬火條件下，均無法有史賓諾多相分解反應與有序 k′ 碳化物形成之原因。此外，在研究中合金中的碳含量增加，所形成中的 k′ 碳化物中碳濃度亦隨之增加。此表示在初始的 γ 相中較高的碳飽和度，將促使在淬火中傾向碳富集 k′ 碳化物形成的趨勢。

[3]、以前的研究顯示，鐵-(7.8-10) wt.%鋁-(28-34) wt.%錳-(0-1.75) wt.% M (M=鈮+釩+鉬+鎢)-(0.85-1.3) wt.%碳合金的淬火微觀組織為單一的沃斯田鐵相，或是沃斯田鐵中存在少量的（鈮，釩）碳的碳化物。依據化學組成，淬火後的合金最大抗拉強度、降伏強度及延伸率，分別為 840~950MPa、410~550 MPa 及 70~57%。基於先前的研究，可以得出一個結論，淬火後的合金於 550℃續經 16 小時時效，強度和延展性會有一個最佳化的組合，此最佳化組合的獲得乃是因為（Fe、Mn)$_3$AlC 碳化物(k′ 碳化物）在沃斯田鐵基地中形成，且未在晶界上析出。當此等合金的延伸率約為 30% 時，其最大抗拉強度、降伏強度分別可達

953~1259MPa、665~1094 MPa。雖然沃斯田鐵系的 FeAlMnC 合金具有

優異的強度及延性，然而在水的環境中，這些合金的耐腐蝕性不佳，不符

工業的應用。為改善耐蝕性，於 FeAlMnC 合金中添加鉻元素，結果顯示

經淬火後的鐵-(7.1-9.1) wt.% 鋁-(29.2-31.3) wt.% 錳-(2.8-6) wt.% 鉻

-(0.88-1.07) wt.% 碳合金，在 3.5% NaCl 溶液中其耐蝕性顯著優於淬火狀

態及時效熱處理的 FeAlMn (M)C 合金。然而，淬火後的 FeAlMnCrC 合金

仍為單一的沃斯田鐵相，可預期與 FeAlMn(M)C 合金淬火後類似，機械性

能強度均較低。此外，以前學者的研究顯示，鐵-(8.7-9) wt.% 鋁-(28.3-30)

wt.% 錳-(5-5.5) wt.% 鉻-(0.7-1) wt.% 碳的合金，於 550～600 ℃ 施予超過

8 小時的時效，除了沃斯田鐵基地中細緻的 k′ 碳化物的形成外，尚有粗

的 $(Fe,Mn,Cr)_7C_3$ 碳化物以異質方式（heterogeneously）於晶界上析出，

此 $(Fe,Mn,Cr)_7C_3$ 碳化物於晶界上析出，導致耐蝕性變差。這意味著以前

的研究中，很難在沃斯田鐵系的 FeAlMn (M) C 和 FeAlMnCrC 合金，同

時具備高強度、高延展性和優良的耐腐蝕性能。因此，本研究的主要目的

是開發新的沃斯田鐵系 FeAlMnCrC 合金，使其具有高強度和高延性，以

及一個適當的耐蝕性。

　　本文的研究，開發出一種新的沃斯田鐵系的鐵-9 wt.% 鋁-28 wt.% 錳-6

wt.% 鉻-1.8 wt.% 碳合金，該合金經淬火後具有顯著的高強度、高延展性

和優良的耐蝕性。其原因乃此合金於淬火時，沃斯田鐵的基地中有細緻的

k′ 碳化物在基地內整合析出，且在表面有鉻和鋁氧化物形成一層鈍化膜。

系列合金設計中，值得注意的是，於 3.5% NaCl 溶液中的腐蝕極化曲線測試，D(6Cr)合金的蝕孔腐蝕電位為 E_{pp}(-25mV)，其遠高於經時效的鐵-(8.7-9) wt.%鋁-(28.3-30) wt.%錳-(5-5.5) wt.%鉻-(0.7-1) wt.%碳合金的(-500~-240mV)，亦高於經回火的商業化麻田散鐵型 AISI 410 不銹鋼的(-250~-100mV)。此外，D(6Cr)合金的拉伸強度亦與時效後的 FeAlMnC 合金以及 AISI 410 相當。

Phase Trasformations, Mechanical Properties and Corrosion Behaviors of Fe-Al-Ti and Fe-Al-Mn Alloys
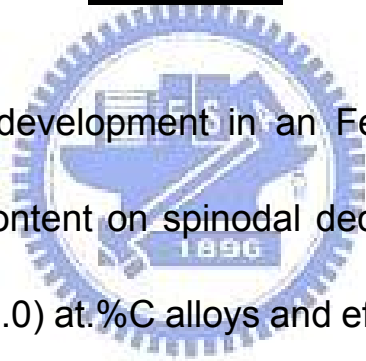
Student: Gow-Dong Tsay   **Advisor: Prof. Tzeng-Feng Liu**

Prof. Chuen-Guang Chao

Department of Materials Science and Engineering

National Chao Tung University

Abstract

The microstructural development in an Fe-24.6 at.%Al-7.5 at.%Ti alloy, effect of carbon content on spinodal decomposition in the Fe-20 at.%Al-26 at.%Mn-(5.0-8.0) at.%C alloys and effect of chromium content on corrosion resistance in Fe-(7.1-9.1) wt.Al-(29.2-31.3) wt.%Mn-(2.8-6) wt.%Cr-(0.88-1.07) wt.%C (Fe-(13.2-16.4) at.%Al-(26.6-27.8) at.%Mn -(2.7-5.6) at.%Cr-(3.7-4.3) at.%C) alloys were examined by means of optical microscopy (OM), transmission electron microscope (TEM), X-ray energy dispersive spectrometer (EDS), X-ray diffractometer (XRD) and Auger electron spectrometer (AES). The results obtained as follows:

[1]. In previous studies, it is seen that the Ti addition in the Fe-Al

binary alloys would (1) strongly increase the $D0_3 \rightarrow B2$ and $B2 \rightarrow A2$ transition temperatures, (2) significantly expand the $(A2+D0_3)$ phase field, and (3) cause the $D0_3$ APBs to exhibit a tendency toward anisotropy. In addition, a $(B2+L2_1)$ ($L2_1$ is the ternary equivalent of the binary $D0_3$ structure.) two-phase field was reported to be existent at temperatures ranging from 1073 to 1273K in the Fe-Al-Ti ternary alloys. It is noted that the $(B2+D0_3)$ two-phase field has not been found by previous workers in the Fe-Al binary alloys before. However, the existence of the $(B2+L2_1)$ two-phase field in the Fe-Al-Ti ternary alloys was determined principally by using X-ray diffraction, differential scanning calorimetry, differential thermal analysis and electron-probe microanalysis. Recently, we have performed transmission electron microscopy (TEM) investigations on the phase transformations of an Fe-23 at.% Al-8.5 at.% Ti alloy aged at 1173K. Consequently, it was found that when the alloy was aged at 1173K for longer times, the $L2_1$ domains grew considerably and an $A2 \rightarrow (A2+L2_1) \rightarrow (B2+L2_1)$ transition occurred at a/2<100>APBs. This feature has never been reported by other workers in the Fe-Al-Ti alloy systems before. Extending the previous work, the purpose of this study is an attempt to examine the microstructural developments of the Fe-24.6 at.% Al-7.5 at.% Ti alloy

aged at 1173K. It is noted that according to the previously established isothermal sections of Fe-Al-Ti ternary alloys at 1173K, the chemical compositions of both the previous alloy and the present alloy are just located in the $(B2+L2_1)$ region. However, the chemical composition of the present alloy is much closer to the $A2/B2/L2_1$ apex than that of the previous alloy.

In the as-quenched condition, the microstructure of the Fe-24.6 at.% Al-7.5 at.% Ti alloy was the mixture of $(A2+L2_1)$ phases. When the as-quenched alloy was aged at 1173K for 6 h, the $L2_1$ domains grew considerably and the B2 phase was formed at a/2<100> APBs as well as the phase separation from well-grown $L2_1$ to $(B2+L2_1^*)$ occurred basically contiguous to the a/2<100> APBs., where $L2_1^*$ is also of $L2_1$-type structure. After prolonged aging at 1173K, the phase separation would proceed toward the inside of the whole well-grown $L2_1$ domains. Consequently, the microstructure of the alloy aged at 1173K for 36 h was essentially the mixture of $(B2+L2_1^*)$ phases.

[2]. The microstructural developments in fully austenitic FeAlMnC alloys, prepared by conventional casting processes, have been extensively studied by many researchers. In these studies, when an alloy with a chemical composition in the range of Fe-(7.8–11.8) wt.%Al

-(28–34.3) wt.%Mn -(0.74–1.3) wt.%C (Fe-(14.2–20.9) at.%Al-(25–30.1) at.%Mn-(3.1–5.2) at.%C) was solution heat-treated in the single austenite (γ) phase (disordered face-centered cubic (fcc)) region and then quenched rapidly, the microstructure of the alloy was single-phase γ. When the as-quenched alloy was aged at 500–550°C for moderate periods of time, fine $(Fe,Mn)_3AlC_X$ carbides (k′ carbides) began to precipitate coherently within the γ matrix. The $(Fe,Mn)_3AlC_X$ carbide has an ordered fcc crystal structure which belongs to the L′1$_2$ type. Recently, we performed transmission electron microscopy observations on the phase transformations of an Fe-9 wt.%Al-30 wt.%Mn-2 wt.%C (Fe -16 at.%Al-26 at.%Mn-8 at.%C) alloy. Consequently, we found that the microstructure of the alloy in the as-quenched condition was γ phase, which contained fine k′ carbides formed within the γ matrix by spinodal decomposition during quenching. This is quite different from that observed in the austenitic FeAlMnC alloys with 3.1≤C≤5.2 at.%, in which fine k′ carbides could only be observed in aged alloys. This finding suggests that the carbon content may play an important role in the formation of fine k′ carbides within the γ matrix during quenching. However, to date, the reason why adding a greater amount of carbon could lead to this result is unclear. Therefore, the main purpose of this

work is to study systematically the effect of carbon content on the as-quenched microstructure of Fe-20 at.%Al-26 at.%Mn-C alloys with 5.0≤C≤8.0 at.%.

The experimental results revealed that spinodal decomposition and formation of ordered k′ carbides could be observed in the Fe-20 at.%Al-26 at.%Mn-C alloys with 5.5≤C≤8.0 at.% under the as-quenched condition. Both the wavelength and the amount of ordered k′ carbides increased with increasing of carbon content, indicating that the temperatures of both spinodal decomposition and ordering reaction increased with increasing carbon content. With increasing carbon content, the lattice parameters of both the ordered k′ carbides and the disordered γ_0 phase increased, whereas the misfit between the two phases decreased. Especially, the coherency strain energy was increased dramatically as the carbon content approached slightly below 5.5 at.%. Given the remarkable increase in strain energy, undercooling may be insufficient to overcome the strain energy effects, which are responsible for the absence of spinodal decomposition and formation of ordered k′ carbides in the present alloy with 5.0 at.% C and in previous austenitic FeAlMnC alloys with 3.1≤C≤5.2 at.% under the as-quenched condition. Additionally, the carbon concentration in the k′ carbides

formed in the present alloys increased with increasing carbon content. This indicates that a higher degree of carbon supersaturation in the initial γ phase might promote a tendency toward C-rich k′ carbides formation during quenching.

[3]. Previous studies have shown that the as-quenched microstructure of the Fe-(7.8-10) wt.%Al-(28-34) wt.%Mn-(0-1.75) wt.% M (M=Nb+V+Mo+W)-(0.85-1.3) wt.%C alloys is single austenite (γ) phase or γ phase with small amounts of (Nb,V)C carbides. Depending on the chemical composition, the ultimate tensile strength (UTS), yield strength (YS), and elongation of the as-quenched alloys ranges from 840 to 950 MPa, 410 to 550 MPa and 70 to 57%, respectively. Based on the results of the previous studies, it can be generally concluded that alloys having an optimal combination of strength and ductility can be obtained when the as-quenched alloys are aged at 550℃ for about 16 h, this optimal combination is obtained because of the formation of fine (Fe,Mn)$_3$AlC carbides (k′ carbides) within the γ matrix and the absence of precipitates on the grain boundaries. These alloys have an elongation better than about 30%, and UTS and YS values of 953~1259 MPa and 665~1094 MPa, respectively. Although the austenitic FeAlMn(M)C alloys possess the remarkable combination of strength and ductility, the

corrosion resistance of these alloys in aqueous environments is not adequate for use in industrial applications. In order to improve the corrosion resistance, chromium has been added to the austenitic FeAlMnC alloys. Consequently, it has been found that the corrosion resistance of the as-quenched Fe-(7.1-9.1) wt.%Al-(29.2-31.3) wt.%Mn -(2.8-6) wt.%Cr-(0.88-1.07) wt.%C alloys becomes considerably better than that of the as-quenched or aged FeAlMn(M)C alloys. However, the as-quenched microstructure of these FeAlMnCrC alloys still remains to be single γ phase. It is thus expected that the mechanical strength of the as-quenched FeAlMnCrC alloys would be low similar to that of the as-quenched FeAlMn(M)C alloys. Furthermore, previous studies on the Fe-(8.7-9) wt.%Al-(28.3-30) wt.%Mn-(5-5.5) wt.%Cr-(0.7-1) wt.%C alloys aged at 550~600℃ for a time period longer than 8 h have indicated that besides the formation of the fine k′ carbides within the γ matrix, the coarse $(Fe,Mn,Cr)_7C_3$ carbides might precipitate heterogeneously on the grain boundaries. The precipitation of the coarse $(Fe,Mn,Cr)_7C_3$ carbides on the grain boundaries results in the corrosion resistance being poor. This implies that it is difficult for the austenitic FeAlMn(M)C and FeAlMnCrC alloys examined in the previous studies to possess both high-strength and high-ductility along with good

corrosion resistance. Therefore, the main aim of this study is to develop new austenitic FeAlMnCrC alloys that possess high-strength and high-ductility as well as an appropriate corrosion resistance.

In this study, a new austenitic Fe-9 wt.%Al-28 wt.%Mn-6 wt.%Cr -1.8 wt.%C alloy is developed. The as-quenched alloy possesses a remarkable combination of high-strength, high-ductility, and moderate corrosion resistance, which is attributed to the presence of fine k′ carbides formed coherently within the γ matrix during quenching and to a layer of Cr and Al oxides in the passive film. The pitting potential E_{pp} (-25 mV) of the alloy measured in 3.5% NaCl solution is noticeably higher than that of the aged FeAlMnC alloys (-500~-240 mV) and the tempered AISI 410 martensitic stainless steel (-250~-100 mV). In addition, the tensile strength of the alloy is comparable to that of the aged FeAlMnC alloys and AISI 410.

Contents

List of Tables

List of Figures

Chapter 1.

General Introduction

General Introduction

Fe-Al alloys are generally used for high-temperature structural applications due to the low cost, reasonable strength and good corrosion resistance [1-3]. However, the application ambit has been limited owing to the low room-temperature ductility and a sharp drop in strength above 873K, which is well-known to be related to the $D0_3 \rightarrow B2$ phase transformation [1]. In order to improve the high-temperature strength, alloying elements was added into the Fe-Al binary alloys as transition metals (Ti, V, Mo, Ze…etc.) for increasing transition temperature. The addition of Ti resulted in a significantly large increase of the $D0_3 \rightarrow B2$ transition temperature about 60K/at% [4-8].

The microstructures of the Fe-Al-Ti ternary alloys have been studied by many workers [8-20]. In the previous studies, it is seen that the Ti addition in the Fe-Al binary alloys would (1) strongly increase the $D0_3 \rightarrow B2$ and $B2 \rightarrow A2$ transition temperatures, (2) significantly expand the $(A2+D0_3)$ phase field, and (3) cause the $D0_3$ APBs to exhibit a tendency toward anisotropy. In addition, a $(B2+D0_3)$ two-phase field was reported to be existent at temperatures ranging from 1073 to 1273K in the Fe-Al-Ti ternary alloys [16-20]. It is worth mentioning that the $(B2+D0_3)$ two-phase field has not been observed by previous workers in the Fe-Al binary alloys

2

before [21-22]. However, the existence of the (B2+D0$_3$) two-phase field in the Fe-Al-Ti ternary alloys was determined mainly by using optical micrography (OM), scanning electron microscopy (SEM), x-ray diffraction (XRD), differential scanning calorimetry (DSC), differential thermal analysis (DTA) and electron-probe microanalysis (EPMA) [16-20].

Recently, Su et al. have performed transmission electron microscopy (TEM) investigations on the phase transformations of Fe-(20-23) at.%Al-(7, 8.5) at.%Ti alloys aged at 1073~1273K [23-25]. Consequently, it was found that the as-quenched microstructure of both the Fe-23 at.%Al-7 at.%Ti and Fe-23 at.%Al- 8.5 at.%Ti alloys was a mixture of (A2+D0$_3$) phases. The (A2+D0$_3$) phases were formed by an A2→B2→(A2+D0$_3$) transition during quenching [23-24]. When the Fe-23at.%Al-7at.%Ti alloy was aged at 1073K for moderate times, the D0$_3$ domains grew preferentially along <100> directions and extremely fine B2 particles occurred at a/2<100> anti-phase boundaries (APBs). After prolonged aging at 1073K, the B2 particles would grow to occupy the whole a/2<100> APBs. As a result, the stable microstructure of the alloy present at 1073K was a mixture of (B2+D0$_3$) phases [23]. Whereas, when the Fe-23at.%Al- 8.5at.%Ti alloy was aged at 1173K for longer times, the D0$_3$ domains existing in the as-quenched alloy grew

3

considerably and an A2→(A2+D0$_3$)→(B2+D0$_3$) transition occurred at a/2<100> APBs of the D0$_3$ domains [24]. These microstructural evolutions have never been reported by other workers in the Fe-Al-Ti alloy systems before. Additionally, we found that when the Fe-23 at.%Al- 8.5 at.%Ti alloy was aged at 1273K, rod-like C14 precipitates could be observed within the (A2+D0$_3$) matrix [25]. Although the C14 precipitate was extensively reported to be observed in the aged Fe-Al-Ti alloys, little information concerning the orientation relationship between the C14 precipitate and matrix has been provide. By using transmission electron microscopy, Su et al. determined the orientation relationship between the C14 precipitate and (A2+D0$_3$) matrix to be $(0001)_{C14}//(\bar{1}\bar{1}2)_m$, $(\bar{1}100)_{C14}//(\bar{1}10)_m$, $(11\bar{2}0)_{C14}//(111)_m$ [25].

Phase transformations, mechanical properties and corrosion resistance in austenitic FeMnAlC alloys have also been studied by many workers [26-59]. In these studies, it is seen that the as-quenched microstructure of the Fe-(6-11.8) wt.%Al-(26-34.3) wt.%Mn-(0-1.75) wt.%M (M=Nb+V+Mo+W)-(0.54-1.3) wt.%C alloys was single-phase austenite (γ) or γ phase with small amount of (Nb,V)C carbides. Depending on the chemical composition, the alloys in the as-quenched condition show various ultimate tensile strength (UTS) ranging from 840

to 950 MPa, yield strength (YS) ranging from 410 to 550 MPa and elongation from 70 to 57% [33, 36-50]. When the as-quenched alloys were aged at 500~750℃ for moderate times, fine $(Fe,Mn)_3AlC$ carbide (κ′ carbide) having an L′1_2-type structure started to precipitate coherently within the γ matrix and no precipitates could be observed on the γ/γ grain boundaries. Based on the previous studies, it can be generally concluded that the alloys could possess an optimal combination of strength and ductility when the as-quenched alloys were aged at 550℃ for about 16 h [33-35, 39]. With an elongation better than about 30%, the values of UTS and YS could be attained to be 953~1259 MPa and 665~1094 MPa, respectively [33-35, 39-40]. After prolonged aging time within this temperature range, the coarse $(Fe,Mn)_3AlC$ carbide (κ carbide) started to precipitate heterogeneously on the γ/γ grain boundaries. The coarse k carbide also has an L′1_2-type structure. Depending on the chemical composition and aging temperature, the coarse k carbides would grow into adjacent γ grains through a γ→α(ferrite)+β-Mn reaction, a γ→$γ_0$ (carbon- deficient austenite)+κ reaction , a γ→β-Mn+κ reaction or a γ→α+β-Mn+κ reaction [30-35]. Due to the formation of the coarse k carbides on the grain boundaries, both of strength and ductility were drastically dropped [36-59].

Although the austenitic FeAlMnC alloys could possess the remarkable combination of strength and ductility, the corrosion resistance of the alloys in aqueous environments was not adequate for applications in industry [60-64]. In order to improve the corrosion resistance, Cr has been added to the austenitic FeAlMnC alloys [63-66]. In these studies, it was found that E_{corr} and E_{pp} of the as-quenched austenitic Fe-(7.1-9.1) wt.%Al-(29.2-31.3) wt.%Mn-(2.8-6) wt.% Cr-(0.88-1.07) wt.%C alloys in 3.5% NaCl solution were ranging from -820 to -556 mV and from -240 to -27 mV, respectively [63-66]. The results were much better than the E_{corr} (-920~-789 mV) and E_{pp} (-500~-280 mV) of the as-quenched austenitic FeAlMnC alloys [60-64].

The effects of Cr addition on the microstructures of the FeAlMnC alloys have also been examined by several workers [67-68]. In the previous study [67], it was reported that when the austenitic Fe-9 wt.%Al-30 wt.%Mn-5 wt.%Cr-0.7 wt.%C alloy was aged at 550-750℃, the fine κ′ carbides were formed within the γ grains, and a $(M_7C_3+D0_3)\rightarrow (M_7C_3+B2)\rightarrow(M_7C_3+\alpha)$ reaction occurred on the γ/γ grain boundaries. Besides, when the austenitic Fe-8.7 wt.%Al-28.3 wt.%Mn-5.5 wt.%Cr-1 wt.%C alloy was aged at 800~1250℃, a $(\gamma+Cr_7C_3)\rightarrow\gamma\rightarrow(\gamma+(\alpha+B2+D0_3))$ reaction occurred within the γ grain and on the γ/γ grain boundaries [68].

In addition to extensive studies of FeAlMnC alloys with C≦1.3 wt.%, the phase transformations and mechanical properties in the FeAlMnC alloys with higher C content have also been examined [69-71]. Recently, Wang et al. performed TEM observation on the phase transformations of an Fe-30wt.%Mn-9wt.%Al-2wt.%C alloy [69]. Consequently, it was found that the as-quenched microstructure of the alloy was γ phase containing fine κ′ carbides. The fine κ′ carbides were formed within the γ matrix by spinodal decomposition during quenching. This is quite different from that observed in the FeAlMnC alloys with C≦1.3wt.%. After being aged at 550~1050℃, the fine κ′ carbides grew and a $\gamma \to \gamma_0 + \kappa$ carbide reaction occurred on the γ/γ grain boundaries [69]. In the as-quenched condition, the UTS, YS and elongation of the Fe-(8.5-9) wt.%Al-(28-30) wt.%Mn-(1.8-2) wt.%C alloys were 1080~1105MPa, 868~883 MPa and 55.5~54.5%, respectively [70-71]. It is obviously seen that with equivalent elongation, the mechanical strength was much higher than that examined in the as-quenched FeAlMnC alloys with C≦1.3wt.%. Furthermore, after being aged at 450~550℃ for 9~12 h, the alloys could possess high UTS ranging from1395 to 1552 MPa and YS ranging from 1262 to 1423 MPa with a good elongation ranging from 32.5 to 25.8% [70-71].

Based on the above literature review, the purposes of the present

thesis are listed as below:

(1) For extending the previous works, the purpose of present study is an attempt to examine the microstructural developments of the Fe-24.6 at.%Al-7.5 at.%Ti alloy aged at 1173K. The detailed experimental results and discussion are presented in Chapter 2.

(2) To date, the reason why higher carbon addition could lead the formation of fine κ' carbides within the γ matrix during quenching is unclear. Therefore, an attempt to study systematically the effect of carbon content on the as-quenched microstructure of the Fe-20 at.%Al-26 at.%Mn-(5.0-8.0) at.%C alloys was performed by using XRD and TEM. The detailed experimental results and discussion are presented in Chapter 3.

(3) According to the previous literatures, it seems to imply that the austenitic FeAlMnC and FeAlMnCrC alloys are difficult to possess both high-strength high-ductility and appropriate corrosion resistance. Therefore, the purpose of present study is an attempt to develop new austenitic FeAlMnCrC alloys possessing high-strength high-ductility and good corrosion resistance simultaneously. The detailed experimental results and discussion are presented in Chapter 4.

References

1. O. Ikeda, I.Ohnuma, R. Kainuma, K. Ishida: Intermetallics 9 (2001) 755.

2. D.G. Morris, M. Leboeuf, S. Gunther, M. Nazmy, Phil Mag A70:1067.

3. C.G. McKamey, J.H DeVan, P.F. Tortorell, V.K. Sikka, J. Mater. Res. 6 (1991) 1779.

4. J. M. Cairney, P.R. Munroe, J. Mater. Sci. Let. 18 (1999) 449.

5. U. Prakash, R.A. Buckley, H. Jones, Mater. Sci. Tech. 9 (1993) 16.

6. Y. Nishino, C. Kumada, S. Asano, Scripta Mater. 36 (1997) 461.

7. Y. Nishino, S. Asano, T. Ogawa, Mater. Sci. Eng. A 234-236 (1997) 271.

8. L. Anthony, B. Fultz, Acta Metall. Mater. 43 (1995) 388.

9. F. Dobeš, P. Kratochvíl, K. Milička, Intermetallics 14 (2006) 1199.

10. S.M. Zhu, K. Sakamoto, M. Tamura, K. Iwasaki, Scripta Mater. 42 (2000) 905.

11. U. Prakash, G. Sauthoff, Intermetallics 9 (2001) 107.

12. F. Stein, A. Schneider, G. Frommeyer, Intermetallics 11 (2003) 71.

13. M. Palm, Intermetallics 13 (2005) 1286.

14. M.G. Mediratta, S.K. Ehlers, H.A. Lipsitt, Metall. Trans. A 18 (1987) 509.

15. O. Ikeda, I. Ohnuma, R. Kainuma, K. Ishida, Intermetallics 9 (2001) 755.

16. M. Palm, G. Sauthoff, Intermetallics 12 (2004) 1345.

17. M. Palm, J. Lacaze, Intermetallics 14 (2006) 1291.

18. G. Ghosh, in: G. Effenberg (Eds.), Ternary Alloy Systems, Springer Berlin Heidelberg, New York, 2005, pp. 426-452.

19. I. Ohnuma, C.G. Schön, R. Kainuma, G. Inden, K. Ishida, Acta Mater. 46 (1998) 2083.

20. S.M. Zhu, K. Sakamoto, M. Tamura, K. Iwasaki, Mater. Trans. JIM. 42 (2001) 484.

21. P.R. Swann, W.R. Duff, R.M. Fisher, Metall. Trans. 3 (1972) 409.

22. S.M. Allen, J.W. Cahn, Acta Metall. 24 (1976) 425.

23. C.W. Su, C.G. Chao, T.F. Liu, Mater. Trans. 48 No.11 (2007) 2993.

24. C.W. Su, C.G. Chao, T.F. Liu, Scripta Mater. 57 (2007) 917.

25. C.W. Su, S.C. Jeng, C.G. Chao, T.F. Liu, Scripta Mater. 57 (2007) 125.

26. K. Sato, K. Tagawa, Y. Inoue, Scripta Metall. 22 (1988) 899.

27. T.F. Liu, J.S. Chou, C.C. Wu, Metal. Trans. A 21 (1990) 1891.

28. K.H. Han, J.C. Yoon, W.K. Choo, Scripta Metall. 20 (1986) 33.

29. C.N. Hwang, T.F. Liu, Scripta Mater. 36 No.8 (1997) 853.

30. C.Y. Chao, C.N. Hwang, T.F. Liu, Scripta Metall. 28 (1993) 109.

31. K. Sato, K. Tagawa, Y. Inoue, Metal. Trans. A 21 (1990) 5.

32. C.N. Hwang, C.Y. Chao, T.F. Liu, Scripta Metall. 28 (1993) 263.

33. W.K. Choo, J.H. Kim, J.C. Yoon, Acta Mater. 45 (1997) 4877.

34. I.S. Kalashnikov, O. Acselrad, A. Shalkevich, J. Mater. Process. Technol. 136 (2003) 72.

35. G.S. Krivonogov, M.F. Alekseyenko and G.G. Solovyeva, Fiz. Metal. Metalloved 39 No.4 (1975) 775.

36. S.C. Tjong, S.M. Zhu, Mater. Trans. 38 No.2 (1997) 112.

37. I.S. Kalashnikov, O. Aksel'rad, M.S. Khadyev, Metal Sci. Heat Treat. 48 (2006) 5.

38. Kalashnikov, O. Acselrad, A. Shalkevich, L.C. Pereira, J. Mater. Eng. Perform. 9 (2000) 597.

39. I.S. Kalashnikov, B.S. Ermakov, O. Aksel'rad, L.K. Pereira, Metal Sci. Heat Treat. 43 No.11-12 (2001) 493.

40. Y. Kimura, K. Handa, K. Hayashi, Y. Mishima, Intermetallics 12 (2004) 607.

41. S.K. Banerji, Met. Prog. (1987) 59.

42. H.W. Leavenworth, Jr. and J.C. Benz, J. Met. (1985) 36.

43. J. Charles, A. Berghezan, A. Lutts, P.L. Dancoisne, Met. Prog. (1981) 71.

44. R. Wang, F.H. Beck, Met. Prog. (1983) 72.

45. J.C. Grcia, N. Rosas, R.J. Rioja, Met. Prog. (1982) 47.

46. D.J. Schmatz, Trans. ASM. 52 (1960) 898.

47. M.F. Alekseyenko, G.S. Krivonogov, L.G. Kozyreva, I.M. Kachanova, L.V. Arapova, Met. Sci. Heat Treat. 14 No.3-4 (1972) 187.

48. L.I. Lysak, M.F. Alekseyenko, A.G. Drachinskaya, N.A. Storchak, G.S. Krivonogov, Metallofizika 59 No.4 (1975) 29.

49. R.E. Cairns, Jr. and J.L. Ham, U.S. patent, No. 3111405 (1963).

50. I. Briggs, G.J. Russell, A.G. Clegg, J. Mater. Sci. 20 (1985) 668.

51. W.K. Choo, K.H. Han, Metall. Trans. A 16 (1985) 5.

52. W.K. Choo, D.G. Kim, Metall. Trans. A 18 (1987) 759.

53. S.C. Tjong, N.G. Ho, Metallography 21 (1988) 199.

54. G.L. Kayak, Met. Sci. Heat Treat. 22 No.2 (1969)95.

55. S.M. Zhu, S.C. Tjong, Metall. Trans. A 29 (1998)299.

56. I.S. Kalashnikov, O. Acselrad, L.C. Pereira, T. Kalichak, M.S. Khadyyev, J. Mater. Eng. Perform. 9 (2000)334.

57. S.C. Tjong, C.S. Wu, Mater. Sci. Eng. 80 (1986) 203.

58. I.F. Tsu, T.P. Perng, Metall. Trans. A 22 (1991) 215.

59. S.M. Zhu, S.C. Tjong, Scripta Mater. 36 (1997) 317.

60. M. Ruscak, T.P. Perng, Corrosion Oct. (1995) 738.

61. W.T. Tsai, J.B. Duh, J.T. Lee, J. Mater. Sci. 22 (1987) 3517.

62. J.B. Duh, W.T. Tsai, J.T. Lee, Corrosion Nov. (1988) 810.

63. S.C. Chang, J.Y. Liu, H.K. Juang, Corrosion 51 No.5 (1995) 399.

64. C.J. Wang, Y.C. Chang, Mater. Chem. Phys. 76 (2002) 151.

65. C.S. Wang, C.Y. Tsai, C.G. Chao, T.F. Liu, Mater. Trans. 48 (2007) 2973.

66. Y.H. Tuan, C.S. Wang, C.Y. Tsai, C.G. Chao, T.F. Liu, Mater. Chem. Phys. 114 (2009) 595.

67. Y.H. Tuan, C.L. Lin, C.G. Chao, T.F. Liu, Mater. Trans. 49 No.7 (2008) 1589.

68. C.M. Liu, H.C. Cheng, C.Y. Chao, K.L. Ou, J. Alloys and Comp. 488 (2009) 52.

69. C.S. Wang, C.N. Hwang, C.G. Chao, T.F. Liu, Scripta Mater. 57 (2007) 809.

70. K.M. Chang, C.G. Chao, T.F. Liu, Scripta Mater. 63 (2010) 162.

71. C.L. Lin, C.G. Chao, H.Y. Bor, T.F. Liu, Mater. Trans. 51 No.6 (2010) 1084.

Chapter 2.

Phase separation from $L2_1$ to $(B2+L2_1)$

in Fe-24.6Al-7.5Ti alloy

Phase separation from $L2_1$ to $(B2+L2_1)$

in Fe-24.6Al-7.5Ti alloy

Abstract

As-quenched microstructure of the Fe-24.6 at.% Al-7.5 at.% Ti alloy was a mixture of $(A2+L2_1)$ phases. When the as-quenched alloy was aged at 1173K for moderate times, the $L2_1$ domains grew considerably and B2 phase was formed at a/2<100> anti-phase boundaries (APBs) as well as phase separation from well-grown $L2_1$ to $(B2+L2_1^*)$ occurred basically contiguous to the APBs, where $L2_1^*$ is also a $L2_1$-type phase. With continued aging at 1173K, the phase separation would proceed toward the whole well-grown $L2_1$ domains. This microstructural evolution has not been reported in the Fe-Al-Ti alloy systems before.
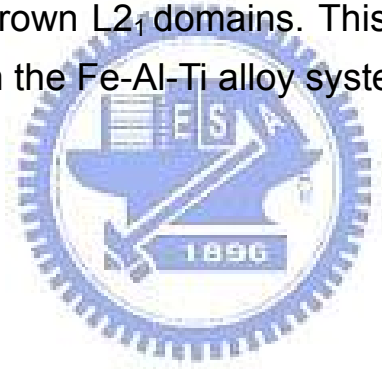
2-1 **Introduction**

In previous studies [1-11], it is seen that the Ti addition in the Fe-Al binary alloys would (1) strongly increase the $D0_3 \rightarrow B2$ and $B2 \rightarrow A2$ transition temperatures [1-10], (2) significantly expand the ($A2+ D0_3$) phase field [5-7], and (3) cause the $D0_3$ APBs to exhibit a tendency toward anisotropy [6]. In addition, a ($B2+ L2_1$) ($L2_1$ is the ternary equivalent of the binary $D0_3$ structure [3].) two-phase field was reported to be existent at temperatures ranging from 1073 to 1273K in the Fe-Al-Ti ternary alloys [7-11]. It is noted that the ($B2+ D0_3$) two-phase field has not been found by previous workers in the Fe-Al binary alloys before [12-13]. However, the existence of the ($B2+ L2_1$) two-phase field in the Fe-Al-Ti ternary alloys was determined principally by using x-ray diffraction, differential scanning calorimetry, differential thermal analysis and electron-probe microanalysis [7-11]. Recently, we have performed transmission electron microscopy (TEM) investigations on the phase transformations of a Fe-23 at.% Al-8.5 at.% Ti alloy aged at 1173K [14]. Consequently, it was found that when the alloy was aged at 1173K for longer times, the $L2_1$ domains grew considerably and an $A2 \rightarrow (A2+ L2_1) \rightarrow (B2+ L2_1)$ transition occurred at a/2<100>APBs. This feature has never been reported by other workers in the Fe-Al-Ti alloy systems before.

Extending the previous work, the purpose of this study is an attempt to examine the microstructural developments of the Fe-24.6 at.% Al-7.5 at.% Ti alloy aged at 1173K. It is noted that according to the previously established isothermal sections of Fe-Al-Ti ternary alloys at 1173K [6-11], the chemical compositions of both the previous alloy and the present alloy are just located in the (B2+ L2$_1$) region. However, the chemical composition of the present alloy is much closer to the A2/B2/L2$_1$ apex than that of the previous alloy.

2-2　Experimental Procedure

The Fe-24.6 at.% Al-7.5 at.% Ti alloy was prepared in a vacuum induction furnace by using Fe(99.9%), Al(99.9%) and Ti(99.9%). After being homogenized at 1523K for 48 h, the ingot was sectioned into 2-mm-thick slices. These slices were subsequently solution heat-treated at 1373K for 1 h and then quenched into room-temperature water rapidly. The aging processes were performed at 1173K for various times in a vacuum heat-treated furnace and then quenched rapidly. TEM specimens were prepared by means of double-jet electropolisher with an electrolyte of 67% methanol and 33% nitric acid. Electron microscopy was performed on a JEOL JEM-2000FX scanning transmission electron microscope (STEM) operating at 200kV. This microscope was equipped with a Link ISIS 300 energy-dispersive X-ray spectrometer (EDS) for chemical analysis. Quantitative analyses of elemental concentrations for Fe, Al and Ti were made with the aid of a Cliff-Lorimer ratio thin section method.

2-3   Results and Discussion

Figure 2.1(a) is a selected-area diffraction pattern of the as-quenched alloy, exhibiting the superlattice reflection spots of the ordered $L2_1$ phase [14-16]. Figures 2.1(b) and (c) are (200) $L2_1$ (or, equivalently, (100) B2) and (111) $L2_1$ dark-field (DF) electron micrographs of the as-quenched alloy, showing the presence of the small B2 domains and fine $D0_3$ domains, respectively [12-13]. In Figures 2.1(b) and (c), it is seen that the sizes of both B2 and $L2_1$ domains are very small, indicating that these domains were formed during quenching [12-13]. In Figure 2.1(b), it is also seen that a high density of extremely fine disordered A2 phase (dark contrast) could be observed within the B2 domains; otherwise, there would be no contrast within these domains by using a (200) superlattice reflection [6]. Accordingly, the as-quenched microstructure of the alloy was a mixture of (A2+ $L2_1$) phases. This is similar to that observed by the present workers in the Fe-23 at.% Al-8.5 at.% Ti alloy quenched from 1373K [14].

Figure 2.2 is a (111) $L2_1$ DF electron micrograph of the alloy aged at 1173K for 3 h, clearly revealing that the $L2_1$ domains grew significantly and a/2<100> APBs were coated with the disordered A2 phase. However,

Figure 2.1(a)

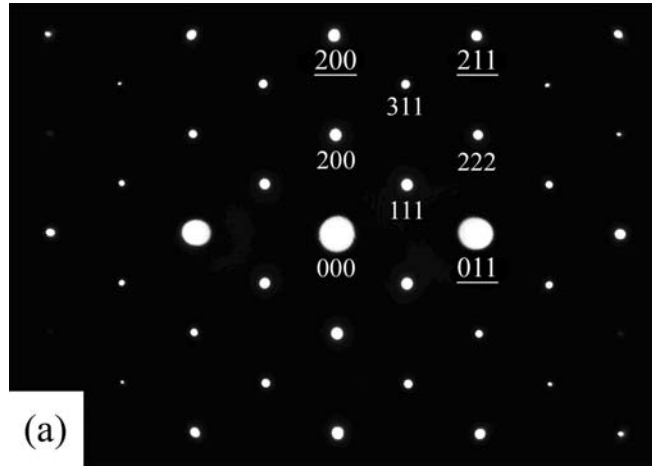

Figure 2.1(b)

(c) 500 nm
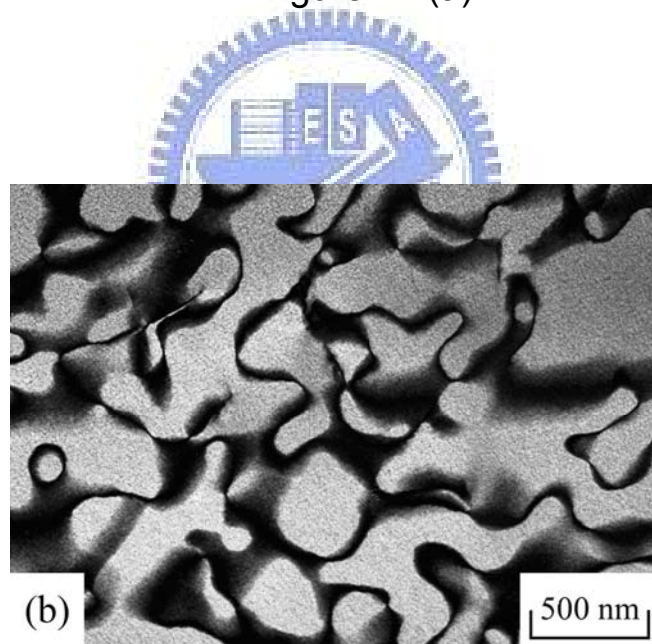
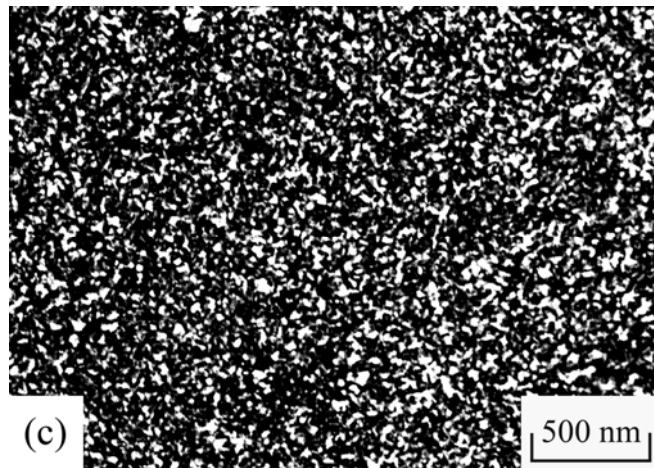Figure 2.1(c)

Figure 2.1 Electron micrographs of the as-quenched alloy: (a) a

selected-area diffraction pattern. The foil normal is [01$\bar{1}$].

(<u>hkl</u>: disordered A2, hkl: L2$_1$ plane); (b) and (c) (200) and
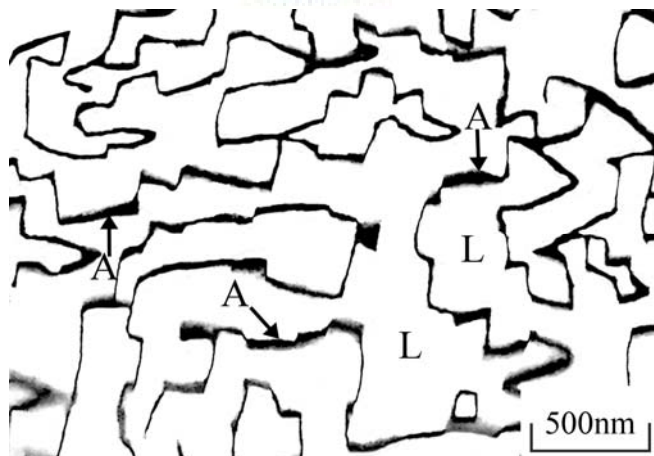
(111) L2$_1$ DF, respectively.

Figure 2.2 (111) L2$_1$ DF electron micrograph of the alloy aged at 1173K

for 3h.

after prolonged aging at 1173K, some tiny particles started to form within the A2 phase. A typical example is shown in Figure 2.3. Figures 2.3(a) and (b) are (111) and (200) $L2_1$ DF electron micrographs of the alloy aged at 1173K for 6 h, showing that the (111) DF image and the (200) DF image are morphologically identical. Therefore, it is likely to conclude that the microstructure of the alloy aged at 1173K for 6 h was also $L2_1$ phase and the a/2<100> APBs were coated with the disordered A2 phase. However, the (111) $L2_1$ DF electron micrograph of the same area as Figure 2.3(a) with a higher magnification revealed that the a/2<100> APBs were fully dark in contrast, as shown in Figure 2.3(c); whereas the (200) $L2_1$ DF electron micrograph showed that some tiny particles (indicated with arrows) could be observed at the a/2<100> APBs, as illustrated in Figure 2.3(d). Therefore, it is reasonable to deduce that the tiny bright particles present in Figure 2.3(d) should be of B2 phase, since the (111) reflection spot comes from the $L2_1$ phase only; while the (200) reflection spot can come from both the $L2_1$ and B2 phases[12-13]. With continued aging at 1173K, the $L2_1$ domains continued to grow and a phase separation started to occur basically contiguous to a/2<100> APBs of the $L2_1$ domains. An example is shown in Figure 2.4. Figure 2.4(a) is a (111) $L2_1$ DF electron micrograph of the alloy aged at 1173K for 12 h, showing that
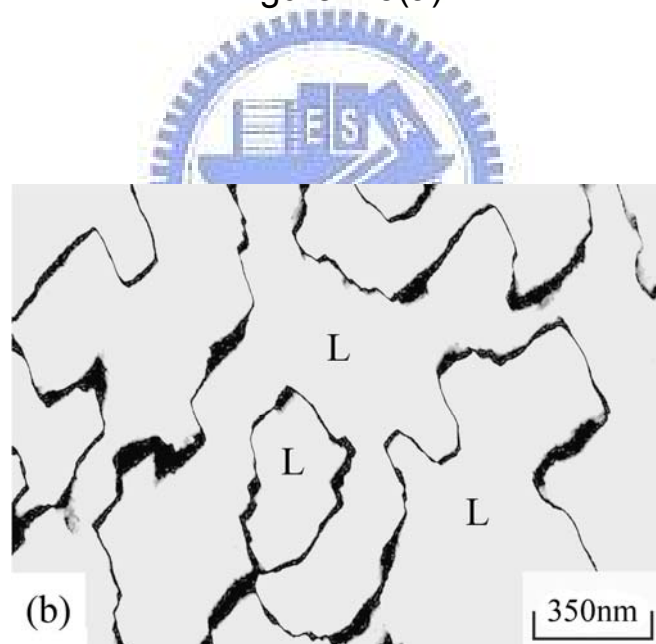
Figure 2.3(a)

Figure 2.3(b)

Figure 2.3(c)

Fig. 2.3(d)

Figure 2.3 Electron micrographs of the alloy aged at 1173 k for 6 h. (a) and (b) (111) and (200) $L2_1$ DF, respectively. (c) and (d) (111) and (200) $L2_1$ DF with a higher magnification of (a) and (b), respectively.

the a/2<100> APBs broadened and well-grown $L2_1$ domains decomposed into fine $L2_1$ domains (designated as $L2_1^*$ phase to be distinguished from the original $L2_1$ phase) separated by dark layers. Figure 2.4(b) is a (200) $L2_1$ DF electron micrograph taken from the same area as Figure 2.4(a), clearly revealing that in addition to the presence of a few A2 particles, the whole region is bright in contrast. This indicates that the broadened dark lines on a/2<100> APBs and dark layers around the periphery of the $L2_1^*$ domains should be of the B2 phase. It is apparent that the B2 phase was formed at a/2<100> APBs and phase separation from $L2_1$ to (B2+ $L2_1^*$) occurred basically contiguous to the a/2<100> APBs. Figure 2.5(a) is a (111) $L2_1$ DF electron micrograph of the alloy aged at 1173K for 24 h, indicating that with increasing aging time, the phase separation would proceed toward the inside of the $L2_1$ domains. Figure 2.5(b), (200) $L2_1$ DF electron micrograph taken from the same area as Figure 2.5(a), clearly reveals that only one a/2<100> APB and one A2 particle (indicated with arrows in Figures 2.5(a) and (b)) could be observed. Figures 2.6(a) and (b) are (111) and (200) $L2_1$ DF electron micrographs of the alloy aged at 1173K for 36 h, revealing that besides a little A2 phase, the well-grown $L2_1$ domains decomposed into the (B2+ $L2_1^*$) phases completely.
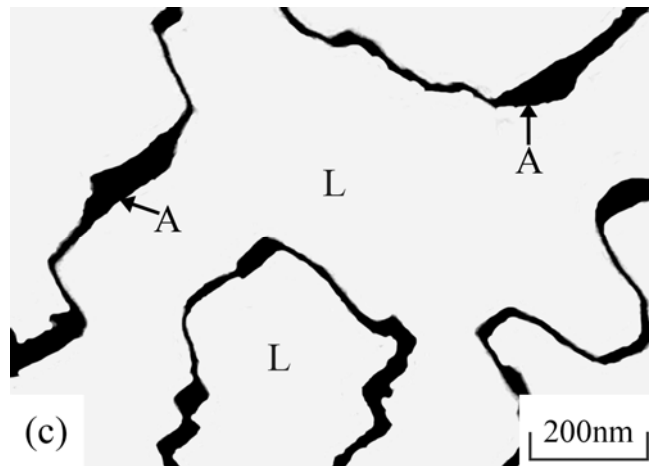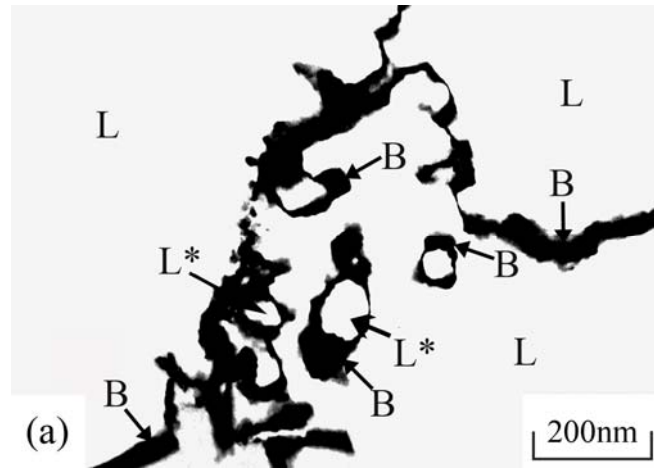
Figure 2.4(a)
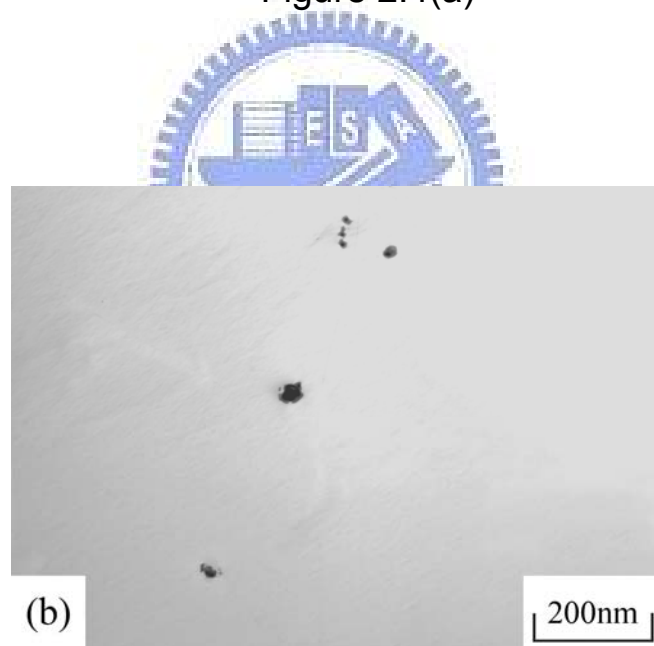
Figure 2.4(b)

Figure 2.4 Electron micrographs of the alloy aged at 1173 k for 12 h.

(a) and (b) (111) and (200) $L2_1$ DF, respectively.
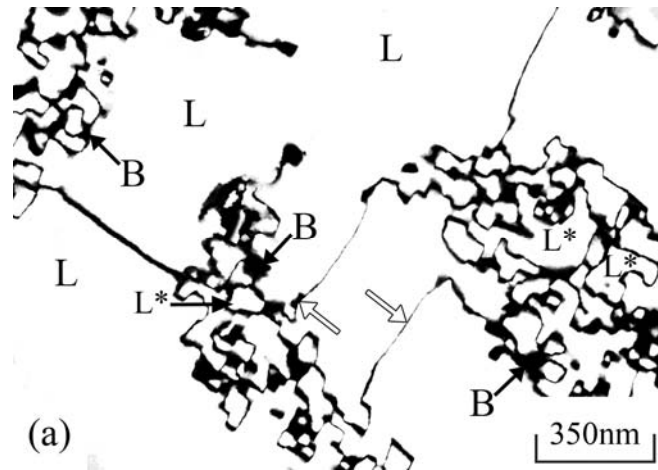
Figure 2.5(a)
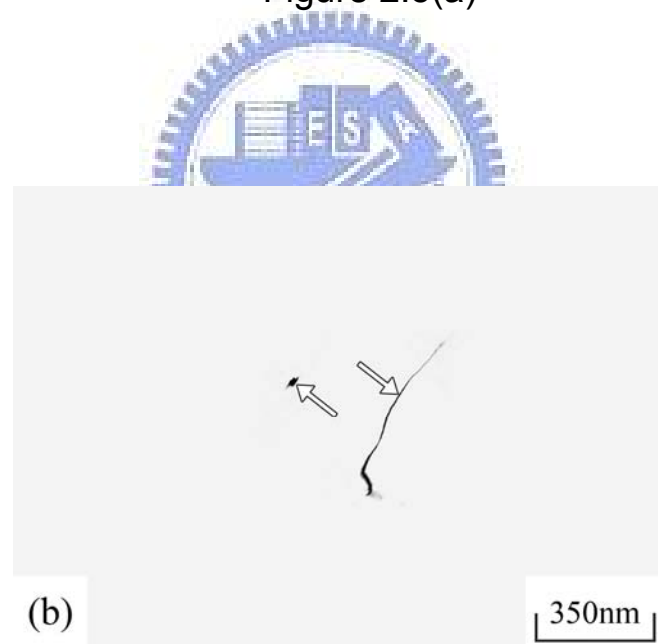
Figure 2.5(b)

Figure 2.5 Electron micrographs of the alloy aged at 1173 k for 24 h.

(a) and (b) (111) and (200) $L2_1$ DF, respectively.
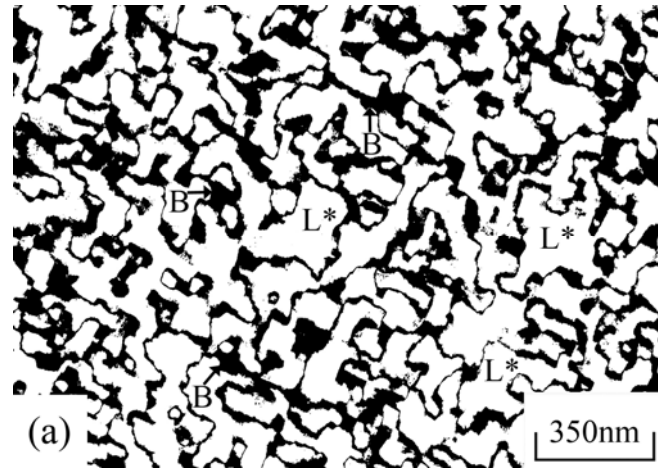
Figure 2.6(a)
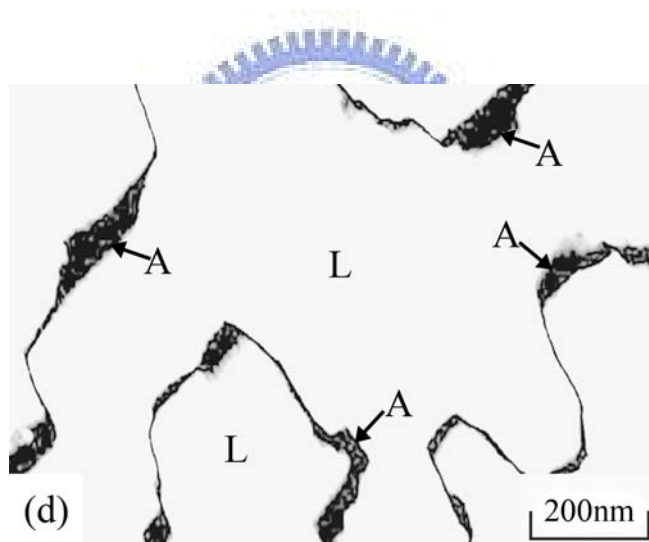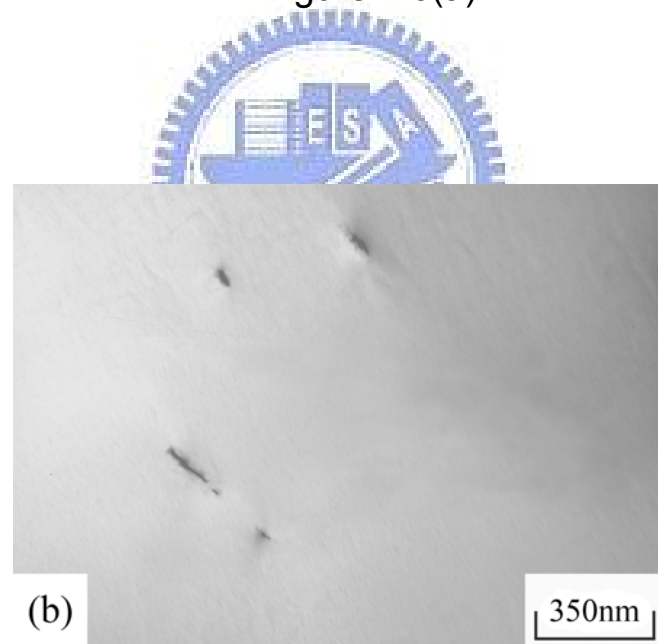

Figure 2.6(b)

Figure 2.6 Electron micrographs of the alloy aged at 1173 k for 36 h.

(a) and (b) (111) and (200) L2$_1$ DF, respectively.

Based on the above observations, some important experimental results are discussed below. When the present alloy was aged at 1173K for moderate times, the B2 phase was formed at a/2<100> APBs and phase separation from well-grown $L2_1$ to (B2+ $L2_1^*$) occurred basically contiguous to the APBs. With increased aging time at 1173K, the phase separation would proceed toward the inside of the whole well-grown $L2_1$ domains. This finding is different from that observed by the present workers in the Fe-23 at.% Al-8.5 at.% Ti alloy[14], in which we have demonstrated that when the Fe-23 at.% Al-8.5 at.% Ti alloy was aged at 1173K, the mixture of the (B2+ $L2_1$) phases occurred at a/2<100> APBs and no evidence of the phase separation could be observed. In order to clarify the apparent difference, an STEM-EDS study was undertaken. The EDS analyses were taken from the areas of the $L2_1$ domains, APBs, B2 phase and $L2_1^*$ domains marked as "L", "A", "B" and "L*" in Figures. 2.2 through 2.6, respectively. The average concentrations of the alloying elements obtained by analyzing at least ten different EDS spectra of each phase are listed in Table 2.1. For comparison, the chemical composition of the as-quenched alloy is also listed in Table 2.1. It is clearly seen in Table 2.1 that when the alloy was aged at 1173K for 3h, the Al and Ti concentrations in the $L2_1$ domains were distinctly higher than those in the

Table 2.1 Chemical compositions of the phases revealed by EDS.

Heat treatment	Phase	Chemical composition (at.%)		
		Fe	Al	Ti
As-quenched	A2+L2$_1$	67.9	24.6	7.5
1173K, 3 h	L2$_1$	65.9	26.2	7.9
	APB(A2)	76.4	19.8	3.8
1173K, 6 h	L2$_1$	66.5	25.7	7.8
	APB(A2+B2)	74.0	22.1	3.9
1173K, 12 h	L2$_1$	67.0	25.2	7.8
	L2$_1^*$	66.2	25.1	8.7
	B2	69.6	24.1	6.3
1173K, 24 h	L2$_1$	67.2	25.1	7.7
	L2$_1^*$	66.2	25.0	8.8
	B2	69.6	24.2	6.2
1173K, 36 h	L2$_1^*$	66.1	25.1	8.8
	B2	69.5	24.2	6.3

as-quenched alloy. This means that along with the growth of the $L2_1$ domains, the concentrations of both Al and Ti at a/2<100> APBs would be lacking. The insufficient concentrations of both Al (19.8 at.%) and Ti (3.8 at.%) would cause the disordered A2 phase to form at a/2<100> APBs, which is consistent with the previously established Fe-Al-Ti phase diagram as shown in Figure 2.7 [10]. According to the phase diagram, the chemical composition of Fe-19.8 at.% Al-3.8 at.% Ti is just located in the A2 phase region. EDS analyses indicated that when the alloy was aged at 1173K for 3-12 h, the Ti concentration in the $L2_1$ domains maintained to be about 7.8 at.% and the Al concentration gradually decreased with increasing the aging time. It is thus expected that the Al atom would proceed to diffuse toward the a/2<100> APBs during aging. In Table 2.1, it is seen that when the alloy was aged at 1173K for 6 h, the Al concentration at a/2<100> APBs increased to 22.1 at.%. The significant increase of the Al concentration would lead the tiny B2 particles to form at a/2<100> APBs, which is also consistent with the Fe-Al-Ti phase diagram in Figure 2.7 [10]. In the phase diagram, it is clearly seen that the chemical composition of Fe-22.1 at.% Al-3.9 at.% Ti is close to the A2/B2 transition boundary. With increasing the aging time, the $L2_1$ domains continued to grow. The quantitative analyses revealed that the Al
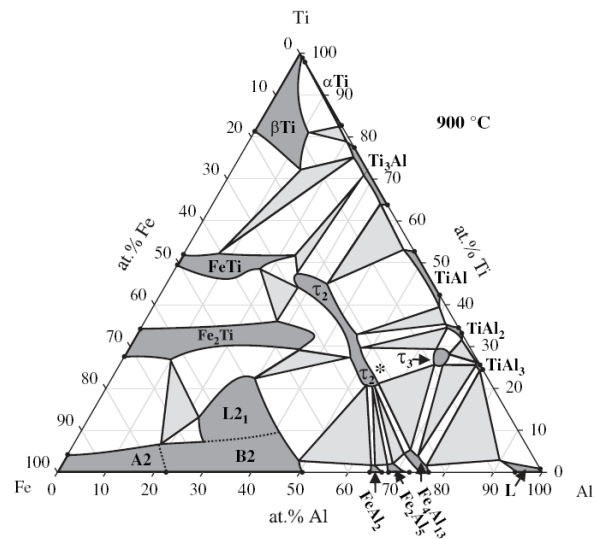
Fig. 2.7 Isothermal section of the Fe-Al-Ti system at 1173K.
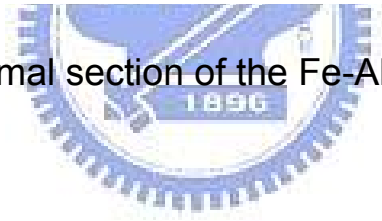
concentration of the L2_1 domains in the alloy aged for 6 h was 25.7 at.%

while that for 12 h was 25.2 at.%, which gave a decrease of only 0.5 at.%.

However, along with the enlargement of the L2_1 domain size, the volume

fraction of the a/2<100> APBs would be lessened considerably. This

means that the slight decrease of the Al concentration in the L2_1 domains

would cause the Al concentration at a/2<100> APBs to increase

appreciably. Therefore, it is reasonable to believe that due to the

appreciable increase of the Al concentration, the A2 phase existing at

a/2<100> APBs would be transformed to B2 phase [10], as observed in

Figure 2.4(a). TEM observations indicated that along with the formation of

the B2 phase, the phase separation from well-grown L2_1 to (B2+ L2_1*)

occurred basically contiguous to a/2<100> APBs. In the following

description, we will attempt to discuss why the well-grown L2_1 domains

underwent the phase separation. In the previous studies, it is well-known

that the D0_3 phase could be found to exist in the Fe-Al binary alloys only

at temperatures below 823K [12-13], and the Ti addition in the Fe-Al

binary alloys would result in a particularly large increase of the D0_3

($L2_1$)→B2 transition temperature about 60K/at.% [6-11]. Obviously, the Ti concentration would be the predominant factor for the stabilization of the $L2_1$ phase at high temperature. In our previous study of the Fe-23 at.% Al-8.5 at.% Ti alloy aged at 1173K for 6-24 h [14], it was found that the Ti concentration in the well-grown $L2_1$ domains was up to about 11.1 at.%, therefore, the $L2_1$ phase exhibited more stable and no evidence of the phase separation could be detected. However, when the present alloy was aged at 1173K for 6-24 h, the Ti concentration in the well-grown $L2_1$ domains was found to be only about 7.8 at.%, which is noticeably lower than that detected in the previous alloy. Therefore, it is plausible to suggest that owing to the lower Ti concentration, the well-grown $L2_1$ domains seemed not very stable at 1173K. Consequently, the well-grown $L2_1$ domains would separate to the mixture of the Ti-riched $L2_1^*$ and Ti-lacked B2 phase, as observed in Figures 2.4 through 2.6.

Finally, three more features are worthwhile to note as follows: (1) In the previous study [14], it is clearly seen that the a/2<100> APBs of the well-grown $L2_1$ domains exhibited more pronounced anisotropy than those observed in the present alloy. The reason is possibly that the well-grown $L2_1$ domains in the previous alloy had significantly higher Ti concentration. (2) The chemical composition of the previous alloy had

higher Ti and lower Al contents [14]. When the previous alloy was aged at 1173K, the $L2_1$ domains grew rapidly and the Ti atom was the major element for diffusing into the a/2<100> APBs. This effect caused the tiny $L2_1$ particles to precipitate preferentially at a/2<100> APBs [14]. However, when the present alloy was aged at 1173K, the Ti concentration in the well-grown $L2_1$ domains maintained to be about 7.8 at.% and the Al atom played the dominant role to diffuse into the a/2<100> APBs. Therefore, the tiny B2 particles were found to form at the a/2<100> APBs, rather than $L2_1$ particles. (3) According to the Fe-Al-Ti phase diagrams [6-11], the A2 phase can not appear for the Fe-24.6 at.% Al-7.5 at.% Ti alloy. However, a little A2 phase was always observed in the present alloy aged at 1173K for 12-36 h. The reason for the difference is plausibly that the phase diagrams were determined by the Fe-Al-Ti alloys heat-treated at 1173K for a time period longer than 336 h, whereas the present alloy was aged for 36 h only. Actually, in the present study, it was found that when the as-quenched alloy was aged at 1173K for 3-36 h, the amount of the A2 phase was indeed decreased with increasing the aging time.

2-4   Conclusions

In the as-quenched condition, the microstructure of the Fe-24.6 at.% Al-7.5 at.% Ti alloy was the mixture of (A2+ $L2_1$) phases. When the as-quenched alloy was aged at 1173K for 6 h, the $L2_1$ domains grew considerably and the B2 phase was formed at a/2<100> APBs as well as the phase separation from well-grown $L2_1$ to (B2+ $L2_1^*$) occurred basically contiguous to the a/2<100> APBs. After prolonged aging at 1173K, the phase separation would proceed toward the inside of the whole well-grown $L2_1$ domains. Consequently, the microstructure of the alloy aged at 1173K for 36 h was essentially the mixture of (B2+ $L2_1^*$) phases.

References

1. Y. Nishino, S. Asano, T. Ogawa, Mater. Sci. Eng. **A 234–236** (1997) 271-274.

2. F. Stein, A. Schneider, G. Frommeyer, Intermetallics **11** (2003) 71-82.

3. M. Palm, Intermetallics **13** (2005) 1286-1295.

4. L. Anthony, B. Fultz, Acta Metall. Mater. **43** (1995) 3885-3891.

5. O. Ikeda, I. Ohnuma, R. Kainuma, K. Ishida, Intermetallics **9** (2001) 755-761.

6. M.G. Mendiratta, S.K. Ehlers, H.A. Lipsitt, Metall. Trans. A **18** (1987) 509-518.

7. I. Ohnuma, C.G. Schon, R. Kainuma, G. Inden, K. Ishida, Acta Mater. **46** (1998) 2083-2094.

8. S.M. Zhu, K. Sakamoto, M. Tamura, K. Iwasaki, Mater. Trans. JIM **42** (2001) 484-490.

9. M. Palm, G. Sauthoff, Intermetallics **12** (2004) 13451359.

10. M. Palm, J. Lacaze, Intermetallics **14** (2006) 1291-1303.

11. G. Ghosh, in: G. Effenberg (Ed.), Ternary Alloy Systems, Springer, Berlin, 2005, pp. 426-452.

12. P.R. Swann, W.R. Duff, R.M. Fisher, Metall. Trans. **3** (1972) 409-419.

13. S.M. Allen, J.W. Cahn, Acta Metall. **24** (1976) 425-436.

14. C.W. Su, C.G. Chao and T.F. Liu: Scr. Mater. **57** (2007) 917-920.

15. S.Y. Yang and T.F. Liu: Scr. Mater. **54** (2006) 931-935.

16. C.H. Chen, T.F. Liu, Metall. Trans. A **34** (2003) 503-509.

Chapter 3.

Effect of Carbon on Spinodal

Decomposition in Fe-20Al-26Mn-C

Alloys

Effect of Carbon on Spinodal Decomposition in Fe-20Al -26Mn-C Alloys

Abstract

The supersaturated austenite (γ) phase decomposed into fine C-rich ordered k′ carbides and C-depleted γ_0 phase during quenching in alloys with 5.5≤C≤8.0 at.%. The misfit between k′ carbides and γ_0 phase decreased with increasing carbon content. The strain energy increased dramatically as carbon content approached slightly below 5.5 at.%. undercooling may be insufficient to overcome the strain energy effects, thus leading to the absence of spinodal decomposition and k′ carbides in the present and prior austenitic FeAlMnC alloys with 3.1≤C≤5.2 at.% under the as-quenched condition. Additionally, both the amount of ordered k′ carbides and the carbon concentration in the k′ carbides increased with increasing carbon content of the alloy. These results revealed that a higher degree of carbon supersaturation in the initial γ phase might promote a tendency toward C-rich k′ particle formation during quenching.

3-1   <u>Introduction</u>

The microstructural developments in fully austenitic FeAlMnC alloys prepared by conventional casting processes have been extensively studied by many researchers [1-11]. In these studies, when an alloy with a chemical composition in the range of Fe-(7.8–11.8) wt.%Al-(28–34.3) wt.%Mn-(0.74–1.3) wt.%C (Fe-(14.2–20.9) at.%Al-(25–30.1) at.% Mn-(3.1–5.2) at.%C) was solution heat-treated in the single austenite (γ) phase (disordered face-centered cubic (fcc)) region and then quenched rapidly, the microstructure of the alloy was single-phase γ [1-11]. When the as-quenched alloy was aged at 500–550 °C for moderate periods of time, fine $(Fe,Mn)_3AlC_X$ carbides (k′ carbides) began to precipitate coherently within the γ matrix [1-11]. The $(Fe,Mn)_3AlC_X$ carbides has an ordered fcc crystal structure which belongs to the L′1_2 type [3-8]. Recently, we performed transmission electron microscopy observations on the phase transformations of an Fe -9 wt.%Al-30 wt.%Mn -2 wt.%C (Fe-16 at.%Al-26 at.%Mn-8at.%C) alloy [12]. Consequently, we found that the microstructure of the alloy in the as-quenched condition was γ phase, which contained fine k′ carbides formed within the γ matrix by spinodal decomposition during quenching. This is quite different from that observed in the austenitic FeAlMnC alloys with 3.1≤C≤5.2 at.%, in

which fine k′ carbides could only be observed in aged alloys [3-11]. This finding suggests that the carbon content may play an important role in the formation of fine k′ carbides within the γ matrix during quenching. However, to date, the reason why adding a greater amount of carbon could lead to this result is unclear. Therefore, the main purpose of this work is to study systematically the effect of carbon content on the as-quenched microstructure of Fe-20 at.%Al-26 at.%Mn-C alloys with 5.0≤C≤8.0 at.%.

3-2 Experimental procedure

Seven alloys, Fe-20at.%Al-26at.%Mn-C (alloys A (5 C), B (5.5 C), C (6 C), D (6.5 C), E (7 C), F (7.5 C), and G (8 C)), were selected for investigation in the present study. The alloys were prepared in a vacuum induction furnace using pure Fe, Mn, Al, and carbon powder. After homogenization at 1250 °C for 12 h under a controlled protective argon atmosphere, the ingots were hot-rolled and then cold-rolled to a final thickness of 2.0 mm. The sheets were subsequently solution heat-treated at 1200 °C for 2 h and then rapidly quenched in room-temperature water. X-ray diffraction (XRD) experiments were carried out by using a Bruker D8 model with Cu-K$_\alpha$ radiation operating at 40 kV and 20 mA. Electron microscopy specimens were prepared by means of a double-jet electropolisher with an electrolyte solution of 10 vol.% perchloric acid, 30 vol.% acetic acid, and 60 vol.% ethanol. Electron microscopy was performed on a JEOL-2100 transmission electron microscope operating at 200 kV. The mean size of the fine k′ particles was determined by a LECO 2000 image analyzer.

3-3 Results and discussion

Figure 3.1 shows the XRD profiles of the seven alloys in the as-quenched condition. The profile of alloy A (5 C) reveals only the fundamental $(200)_\gamma$ reflection. However, sideband peaks around the $(200)_\gamma$ reflection could be observed in alloys B (5.5 C) through G (8 C). The peak appearing on the low-angle side was the $(200)_{k'}$ reflection of C-rich k′ carbides, whereas that appearing on the high-angle side was the $(200)_{\gamma 0}$ reflection of the C-depleted γ_0 phase[9]. The presence of sidebands demonstrates that the ordered C-rich k′ carbides and C-depleted γ_0 phase were formed through spinodal decomposition during quenching in alloys with 5.5≤C≤8.0 at.% [5-7,9]. Moreover, the intensity of the $(200)_{k'}$ peak increased with increasing carbon content, and the $(200)_\gamma$, $(200)_{k'}$, and $(200)_{\gamma 0}$ peaks all shifted to smaller Bragg angles. This indicates that the amount of k′ particles, as well as all the lattice parameters of γ, k′ carbides, and γ_0 phases, increased with increasing carbon content. It is also shown in Figure 3.1 that with increasing carbon content, the sidebands moved closer to the main $(200)_\gamma$ peak, indicating that differences in the parameters between k′ carbides and γ_0 phase decreased. The experimental data above measured from the XRD profiles are listed in Table 3.1. The misfit $(\delta_{k'-\gamma 0})$ was calculated using the equation:
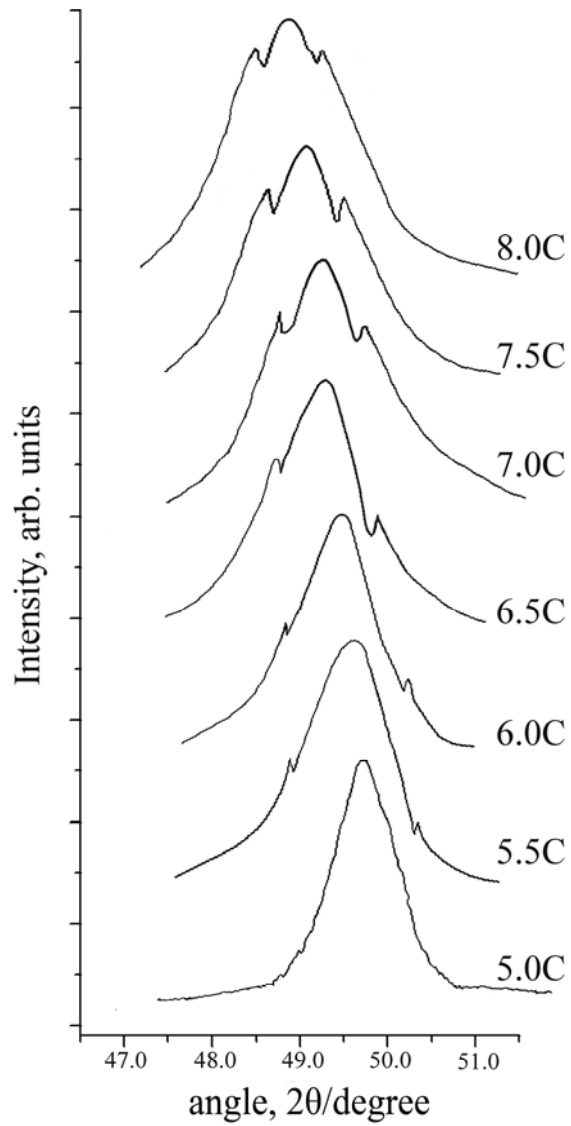
Figure 3.1 X-ray diffraction profiles around the (200)$_\gamma$ Bragg reflection for

the present seven alloys.

$$\delta_{k'-\gamma_0} = 2\left|\frac{a_{k'} - a_{\gamma_0}}{a_{k'} + a_{\gamma_0}}\right| \tag{1}$$

For comparison, the misfit $\delta_{k'-\gamma}$ was also calculated. Both are listed

in Table 3.1. The modulation wavelength was determined using the

Daniel-Lipson equation [6-9]:

$$\lambda = \frac{ha_\gamma \tan\theta}{\Delta\theta(h^2 + k^2 + l^2)} \tag{2}$$

where λ = the average modulation wavelength; θ = the Bragg angle

for the γ peak; $\Delta\theta$ = the angular spacing between the sideband and the

main $(200)_\gamma$ Bragg peak; and h, k, l = the Miller indices of the Bragg peak

(h = 2, and k, l = 0). From Table 3.1, it is clear that increasing the carbon

content causes the misfit to decrease and the wavelength to increase.

Figures 3.2a through c show selected-area diffraction patterns

(SADPs) of alloys A (5 C), D (6.5 C), and G (8 C), respectively. In addition

to the fundamental $(200)_\gamma$ diffraction spot, neither the diffraction spot of

ordered k′ carbides nor the satellites could be detected in alloy A (5 C).

However, both the ordered k′ carbides diffraction spot and satellites could

clearly be observed in alloys D (6.5 C) and G (8 C). Evidently, spinodal

decomposition and formation of ordered k′ carbides occurred during

quenching. In Figures 3.2b and c, it is also seen that in alloy G (8 C),

which has a higher carbon content, the $(100)_{k'}$ spot is relatively brighter
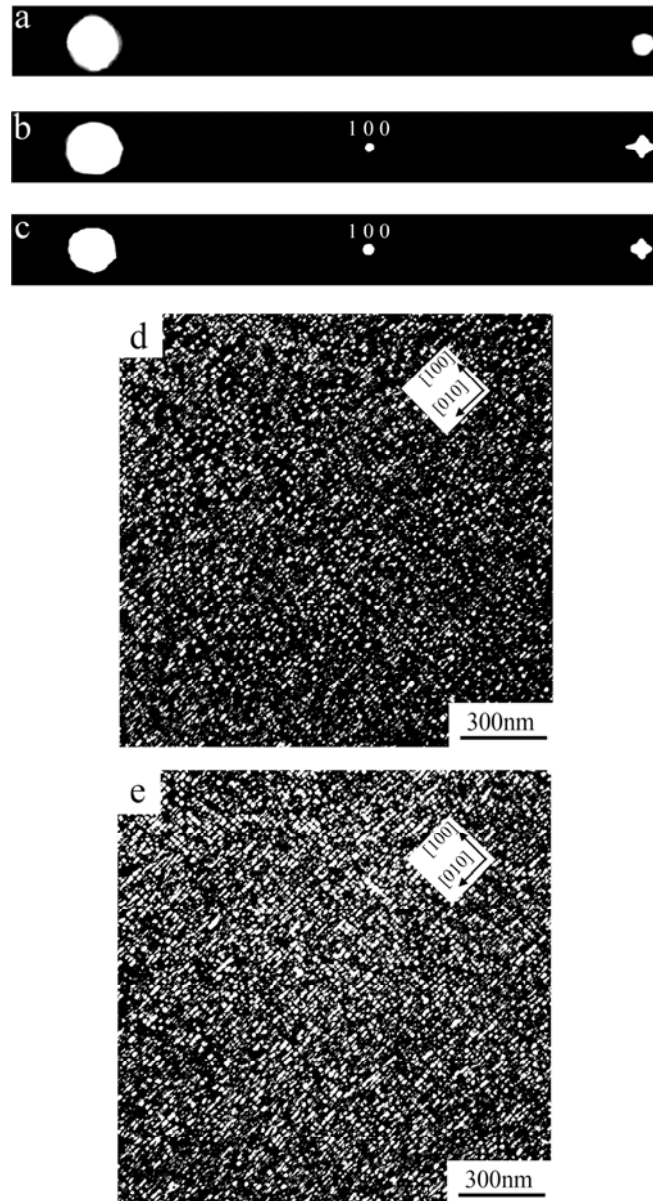
Figure 3.2 Transmission electron micrographs of the present alloys in the as-quenched condition. (a)-(c) SADPs of alloys A (5 C), D(6.5 C), and G (8 C), respectively. （hkl: k′ carbides）, (d)-(e) $(100)_{k'}$ DF images of alloys D (6.5 C) and G (8 C), respectively.

and the spacing between satellites and the main spot is comparatively smaller. The misfit ($\delta_{k'-\gamma_0}$) and wavelength (λ), obtained from measurements of the spacing between the satellites and the main spot along the [100] direction in the SADPs, were 2.24% and 15.7 nm for alloy D (6.5 C), as well as 1.59% and 22.3 nm for alloy G (8 C), respectively. Figures 3.2d and e are two dark-field (DF) electron micrographs taken with the $(100)_{k'}$ superlattice reflection in the [001] zone. They reveal that the amount of ordered k′ carbides in alloy G (8 C) was significantly greater than that in alloy D (6.5 C). In these figures, it is also seen that fine k′ carbides were formed along the <100> direction, consistent with the appearance of the satellites along the <100> reciprocal lattice directions in Figures 3.2b and c. These results obtained by TEM were in good agreement with those investigated by XRD. Image analyses of Figures 3.2d and e indicated that the mean sizes of fine k′ carbides formed in alloys D (6.5 C) and G (8 C) were about 6 and 11 nm, respectively. A detailed TEM examination revealed that although the values of misfit ($\delta_{k'-\gamma_0}$) in alloys D (6.5 C) and G (8 C) reached 2.24 and 1.59%, respectively, no misfit dislocations could be observed on the interface between the k′ carbides and the γ_0 phase. The reason is probably that the fine k′ carbides are very small. According to the values

of misfit ($\delta_{k'-\gamma_0}$), the expected distances between two misfit dislocations in alloys D (6.5 C) and G (8 C) were calculated to be about 16.6 and 23.6 nm, respectively, which is much larger than the size of the k' carbides.

Based on the preceding results, some discussion is appropriate. The microstructure of the present alloy A (5 C) in the as-quenched condition was single-phase γ, which is similar to that observed in as-quenched austenitic FeAlMnC alloys with 3.1≤C≤5.2 at.% [1-11]. However, spinodal decomposition and formation of ordered k' carbides occurred during quenching in the present alloys with 5.5≤C≤8.0 at.%. Regarding spinodal decomposition, two important factors should be considered: (1) interfacial energy effects, and (2) coherency strain energy effects [13]. The k' carbides is a fcc-based phase of L'1$_2$ ordered crystal structure with a C atom at the body center site, an Al atom at the corner positions, and three (Fe, Mn) atoms positioned randomly at the face center sites in its fcc-based unit cell [8]. On the other hand, γ_0 is a disordered fcc phase with C atoms positioned randomly at the octahedral interstitial sites. As the γ_0 phase and ordered k' carbides have the same fcc-based crystal structure and similar lattice parameters, their interface would be fully coherent. Therefore, only chemical contributions should be considered to the interfacial energy [13]. The carbon concentration in the equilibrium

$(Fe,Mn)_3AlC_X$ carbides of austenitic FeAlMnC alloys aged at 500–550 °C for longer times has been studied by several workers. Consequently, three different values of X have been obtained (0.4, 0.6, and 0.66) [6,9,11]. Furthermore, to the authors' knowledge, no information concerning the interfacial energy between the γ_0 phase and ordered k′ carbides has been provided in previous studies. Additionally, in the early stage of spinodal decomposition, the composition fluctuation profile exhibited a sinusoidal wave [6,14]. Therefore, a conclusive description of the interfacial energy between the γ_0 phase and ordered k′ carbides cannot be given in the present study.

Since the composition ratio of (Fe, Mn) and Al in all of the present alloys approximates that of $(Fe,Mn)_3AlC_X$ carbides, it is plausible to suggest that the composition fluctuation was primarily due to the carbon atom. As is evident from the experimental results above, all the lattice parameters of the phases increased with increasing carbon content of the alloy. This suggests that the carbon concentration in these phases increased simultaneously. However, the carbon contribution to the increase in the lattice parameter of the ordered k′ carbides is distinctively less than in the disordered γ_0 phase [15]. Therefore, although all the lattice parameters of the phases increased with increasing carbon content,

the increment in the disordered γ_0 phase was larger than that in the ordered k′ carbides. Consequently, the misfit between the ordered k′ carbides and disordered γ_0 phase would be reduced with increasing carbon content, which is consistent with the results obtained by XRD and TEM. To emphasize the characteristics, the variations in the lattice parameters and misfits as a function of carbon content are plotted in Figure 3.3. For a fully coherent interface, the coherency strain energy would be roughly proportional to δ^2 [13]. In Table 3.1, it is clearly seen that the $\delta^2_{k'-\gamma_0}$ in alloy G (8 C) is only 2.424, whereas that in alloy B (5.5 C) is 8.638. This indicates that the strain energy in alloy B (5.5 C) is about 3.56 times that of alloy G (8 C). The average change in $\delta^2_{k'-\gamma_0}$ between two adjacent alloys ($\Delta\delta^2_{k'-\gamma_0}$/0.5 at.%) was calculated from Table 3.1. In terms of our calculations, it was found that the values between alloys B (5.5 C)-C (6 C), alloys C (6 C)-D (6.5 C), alloys D (6.5 C)-E (7 C), alloys E (7 C)-F (7.5 C), and alloys F (7.5 C)-G (8 C) were about 4.261, 3.406, 2.260, 1.406, and 1.096, respectively, which corresponds to a ratio of 3.89: 3.11: 2.06: 1.28: 1. This means that the average increment of strain energy per decrement of at.% C between 6 and 5.5 at.% C is 3.89 times greater than that between 8 and 7.5 at.% C. The variation in $\delta^2_{k'-\gamma_0}$ with carbon content is also plotted in Figure 3.3. The dotted line shows the expected values
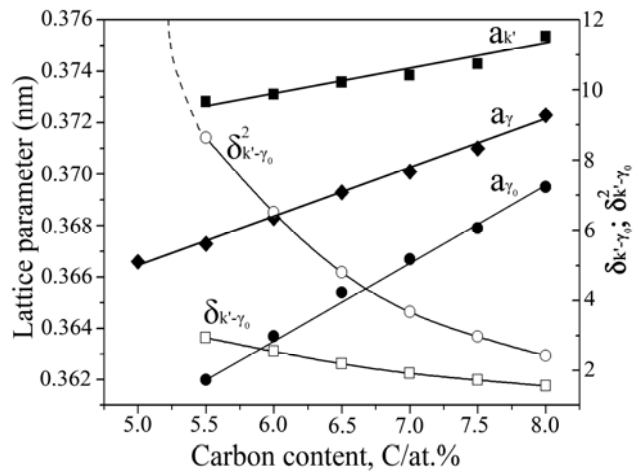
Figure 3.3 Variations in the lattice parameters of k′(■), γ (◆), and γ_0 (●)

phases, as well as $\delta_{k'-\gamma 0}$ (□) and $\delta^2_{k'-\gamma 0}$ (○), as a function of the

carbon content.

Table 3.1. Experimental data obtained from the X-ray diffraction profiles of

the present seven alloys.

Alloy		A	B	C	D	E	F	G
C at.%	Nominal	5	5.5	6.0	6.5	7.0	7.5	8.0
	Virtual	4.98	5.54	6.03	6.52	6.97	7.48	8.02
2θ	k'	—	48.816	48.777	48.722	48.676	48.615	48.468
	γ	49.7	49.600	49.461	49.311	49.192	49.073	48.882
	γ_0	—	50.364	50.125	49.88	49.688	49.511	49.276
Lattice parameter	$a_{k'}$ (nm)	—	0.3728	0.3731	0.3735	0.3738	0.3743	0.3753
	a_{γ} (nm)	0.3666	0.3673	0.3683	0.3693	0.3701	0.3710	0.3723
	a_{γ_0} (nm)	—	0.3620	0.3637	0.3654	0.3667	0.3679	0.3695
Misfit δ (%)	$\delta_{k'-\gamma_0}$	—	2.939	2.551	2.192	1.917	1.724	1.557
	$\delta_{k'-\gamma}$	—	1.486	1.294	1.130	0.994	0.885	0.802
δ^2	$\delta^2_{k'-\gamma_0}$	—	8.638	6.508	4.805	3.675	2.972	2.424
	$\delta^2_{k'-\gamma}$	—	2.208	1.674	1.277	0.988	0.783	0.643
Wavelength (nm)		—	12.40	14.20	16.49	18.81	21.18	23.42
$C_{k'}$ (at.%)		—	11.08	11.59	12.27	12.78	13.63	15.32
(FeMn)$_3$AlC$_x$		—	X=0.50	X=0.53	X=0.56	X=0.59	X=0.63	X=0.73

extrapolated from the $\delta^2_{k'-\gamma_0}$ — C plot. It is evident that the slope of the $\delta^2_{k'-\gamma_0}$

— C curve increased gradually with decreasing carbon content from

8.0 at.% C, and became very steep as the carbon content approached

concentrations slightly below 5.5 at.%. Accordingly, it is reasonable to

expect that a small amount of decrease in carbon content below 5.5 at.%

would cause the coherency strain energy to increase dramatically. As a

result, undercooling may be insufficient to overcome the strain energy

effects. Consequently, spinodal decomposition was completely

suppressed and not detected in the present alloy A (5 C). In addition, the

experimental results revealed that both the wavelength and the amount of

ordered k′ carbides increased with increasing carbon content. This

suggests that the temperatures of both spinodal decomposition and

ordering reaction increased with increasing carbon content.

In previous studies, it was seen that when austenitic FeAlMnC alloys

with 3.1≤C≤5.2 at.% were solution heat-treated at 980–1050 °C and then

rapidly quenched in room-temperature water or ice water, the

microstructure was single-phase γ [1-11]. When the as-quenched alloy

was aged at 500–550 °C, both spinodal decomposition and formation of

ordered k′ carbides could be detected during the early stage of isothermal

aging [3-11]. Han et al. proposed that ordered k′ carbides nucleate in C-rich zones of the γ matrix after undergoing spinodal decomposition [4]. In contrast to this proposition, Choo et al. claimed that spinodal decomposition and formation of ordered k′ carbides occurred concurrently within the γ matrix during aging [8]. Additionally, depending on the chemical composition, aging temperature, and aging time, the wavelength was determined in the range of 23 to 35 nm [6~9]. In spite of the different propositions for the process of spinodal decomposition and ordering, it can generally be concluded that austenitic FeAlMnC alloys with 3.1≤C≤5.2 at.% also lay within the spinodal, and that spinodal decomposition and formation of ordered k′ carbides can only be detected in the alloys during isothermal aging. However, in the present alloys with 5.5≤C≤8.0 at.%, spinodal decomposition and formation of ordered k′ carbides could occur during quenching. The apparent difference may be attributed to the following two reasons: (I) the effect of strain energy between the k′ carbides and γ_0 phase, as discussed above, and (II) the degree of carbon supersaturation in the initial γ phase. As mentioned above, the lattice modulation that occurred in the present alloys is mainly caused by concentration fluctuations in the carbon atom, and the lattice parameter of k′ carbides increased with increasing carbon content of the

alloy. The carbon concentration in k′ carbides can be estimated using the equation [15]: $a_{k'} = 0.36626 + 0.00059C_x$, where the lattice parameter $a_{k'}$ and carbon concentration C_x are presented in nanometers and atomic percent, respectively. The calculated results are also listed in Table 1. It is clear from the table that by increasing the carbon content of the alloy from 5.5 to 8.0 at.%, the carbon concentration in k′ carbides gradually increased from 11.08 at.% (X = 0.50) to 15.32 at.% (X = 0.73). It is evident that a higher degree of carbon supersaturation in the initial γ phase would increase not only the amount of fine k′ carbides but also the carbon concentration in the k′ carbides. Interestingly, it is noted here that the carbon concentrations of 11.08–15.32 at.% (X = 0.50–0.73) are comparable to the values of 9–13 at.% (X = 0.4–0.66) reported by other workers in austenitic Fe-(14–20) at.%Al-(27–30) at.%Mn-(3.7–5) at.%C alloys aged at 500–550 °C for longer periods of time [6,9,11].

Finally, it is worth pointing out that no information concerning the spinodal decomposition curve of the FeAlMnC alloy system has been provided in the literature. Clearly, additional work is needed to further understand the effects of carbon content on spinodal decomposition and ordering in austenitic FeAlMnC alloys.

3-4 <u>Conclusions</u>

In summary, spinodal decomposition and formation of ordered k′ carbides were observed in the present Fe-20 at.%Al-26 at.%Mn-C alloys with 5.5≤C≤8.0 at.% under the as-quenched condition. The gradual increase in both the wavelength and the amount of ordered k′ carbides indicates that the reaction temperatures of both spinodal decomposition and ordering increased with increasing carbon content. With increasing carbon content, the lattice parameters of both the ordered k′ carbides and the disordered γ_0 phase increased, whereas the misfit between the two phases decreased. The coherency strain energy was expected to increase dramatically as the carbon content approached slightly below 5.5 at.%. Given the remarkable increase in strain energy, undercooling may be insufficient to overcome the strain energy effects, which are responsible for the absence of spinodal decomposition and formation of ordered k′ carbides in the present alloy A (5 C) and in previous austenitic FeAlMnC alloys with 3.1≤C≤5.2 at.% under the as-quenched condition. Additionally, the carbon concentration in the k′ carbides formed in the present alloys increased with increasing carbon content. This indicates that a higher degree of carbon supersaturation in the initial γ phase might promote a tendency toward

C-rich k′ carbide formation during quenching.

References

1. Kalashnikov, O. Acselrad, A. Shalkevich, L.C. Pereira: J. Mater. Eng. Perform. 9 (2000) 597-602.

2. K.H. Han: Mater. Sci. Eng. A 279 (2000) 1-9.

3. Acselrad, A.R. de Souza, I.S. Kalashnikov, S.S. Camargo Jr.: Wear 257 (2004) 999-1005.

4. K.H. Han, J.C. Yoon, K.W. Choo: Scripta Metall. 20 (1986) 33-36.

5. I.S. Kalashnikov, O. Acsrlrad, A. Shalkevich, L.D. Chumakova, L.C. Pereira: J. Mater. Process. Tech. 136 (2003) 72-79.

6. K. Sato, K. Tagawa, Y. Inoue: Metall. Trans. A 21A (1990) 5-11.

7. K.H. Han, W.K. Choo, D.E. Laughin: Scripta Metall. 22 (1988) 1873-1878.

8. W.K. Choo, J.H. Kim, J.C. Yoon: Acta Mater. 45 (1997) 4877-4885.

9. K. Sato, K. Tagawa, Y. Inoue: Mater. Sci. Eng. A 111 (1989) 45-50.

10. G.S. Krivonogov, M.F. Alekseyenko, G.G. Solov'yeva: Fitz. Metal. Metalloved 39 No.4 (1975) 775-781.

11. N.A. Storchak, A.G. Drachinskaya: Fitz. Metal. Metalloved 44 No.2

(1977) 373-380.

12. C.S. Wang, C.N. Hwang, C.G. Chao, T.F. Liu: Scripta Mater. 57 (2007) 809-812.

13. D.A. Porter, K.E. Easterling, M. Sherif: *Phase Transformations in Metals and Alloys 3rd Ed.*, (Nelson Thornes Ltd, Cheltenham, 2009), pp308-314.

14. B. Ditchek, L.H. Schwartz: Acta Metall. 28 (1980) 807-822.

15. W.K. Choo, K.H. Han: Metal. Trans. A 16A (1985) 5-10.

Chapter 4.

A New Austenitic FeAlMnCrC Alloy

with High-Strength, High-Ductility,

and Moderate Corrosion Resistance

A New Austenitic FeAlMnCrC Alloy with High-Strength, High-Ductility, and Moderate Corrosion Resistance

Abstract

In this study, a new austenitic Fe-9 wt.%Al-28 wt.%Mn-6 wt.%Cr-1.8 wt.%C alloy is developed. Because the alloy contains a high density of fine $(Fe,Mn)_3AlC$ carbides within the austenite matrix, the alloy in the as-quenched condition exhibits an excellent combination of strength and ductility comparable to that of the aged FeAlMnC alloys. In addition, owing to the formation of a layer of Cr and Al oxides in the passive film formed on the alloys, the corrosion potential E_{corr} (-538 mV) and the pitting potential E_{pp} (-25 mV) of the present alloy in 3.5% NaCl solution are considerably higher than the E_{corr} (-920~-789 mV) and E_{pp} (-500~-240 mV) values of the as-quenched and aged FeAlMnC alloys. Whereas the tensile strength of the present alloy is almost the same as that of conventional AISI 410 martensitic stainless steel, the present alloy possesses superior ductility than AISI 410 martensitic stainless steel. Furthermore, in 3.5% NaCl solution, the E_{pp} (-25 mV) of the present alloy is noticeably higher than that (-250~-100 mV) of the conventional AISI

410 martensitic stainless steel. These results indicate that the present

alloy in the as-quenched condition can possess high-strength and

high-ductility as well as moderate corrosion resistance.

4-1　Introduction

Previous studies have shown that the as-quenched microstructure of the Fe-(7.8-10) wt.%Al-(28-34) wt.%Mn-(0-1.75) wt.%M (M=Nb+V+Mo+ W)-(0.85-1.3) wt.%C alloys is single austenite (γ) phase or γ phase with small amounts of (Nb,V)C carbides [1-10]. Depending on the chemical composition, the ultimate tensile strength (UTS), yield strength (YS), and elongation of the as-quenched alloys ranges from 840 to 950 MPa, 410 to 550 MPa and 70 to 57%, respectively [3-5]. Based on the results of the previous studies, it can be generally concluded that alloys having an optimal combination of strength and ductility can be obtained when the as-quenched alloys are aged at 550℃ for about 16 h, this optimal combination is obtained because of the formation of fine (Fe,Mn)$_3$AlC carbides (k′ carbides) within the γ matrix and the absence of precipitates on the grain boundaries [5-8]. These alloys have an elongation better than about 30%, and UTS and YS values of 953~1259 MPa and 665~1094 MPa, respectively [5-9]. Although the austenitic FeAMnl(M)C alloys possess the remarkable combination of strength and ductility, the corrosion resistance of these alloys in aqueous environments is not adequate for use in industrial applications [1-15]. In order to improve the

corrosion resistance, chromium has been added to the austenitic FeAlMnC alloys [14-17]. Consequently, it has been found that the corrosion resistance of the as-quenched Fe-(7.1-9.1) wt.%Al-(29.2-31.3) wt.%Mn-(2.8-6) wt.%Cr-(0.88-1.07) wt.%C alloys becomes considerably better than that of the as-quenched or aged FeAlMn(M)C alloys [14-17]. However, the as-quenched microstructure of these FeAlMnCrC alloys still remains to be single γ phase [14-17]. It is thus expected that the mechanical strength of the as-quenched FeAlMnCrC alloys would be low similar to that of the as-quenched FeAlMn(M)C alloys. Furthermore, previous studies on the Fe-(8.7-9) wt.%Al -(28.3-30) wt.%Mn-(5-5.5) wt.%Cr-(0.7-1) wt.%C alloys aged at 550~600℃ for a time period longer than 8 h have indicated that besides the formation of the fine k′ carbides within the γ matrix, the coarse $(Fe,Mn,Cr)_7C_3$ carbides might precipitate heterogeneously on the grain boundaries [18,19]. The precipitation of the coarse $(Fe,Mn,Cr)_7C_3$ carbides on the grain boundaries results in the corrosion resistance being poor [16,17]. This implies that it is difficult for the austenitic FeAlMn(M)C and FeAlMnCrC alloys examined in the previous studies to possess both high-strength and high-ductility along with good corrosion resistance. Therefore, the main aim of this study is to develop new austenitic FeAlMnCrC alloys that possess high-strength and

high-ductility as well as an appropriate corrosion resistance.

4-2 Experimental procedure

In this study, the properties of five FeAlMnCrC alloys were investigated. Alloy A (0Cr) contained 28.1% Mn, 9.1% Al, 1.8% C, and balance Fe. Alloys B (3Cr), C (5Cr), D (6Cr), and E (8Cr) contained nearly the same amount of Mn, Al, and C, but contained different amounts Cr, i.e. 3.1, 5.0, 6.1 and 8.2%, respectively. The alloys were prepared in a vacuum induction furnace by using pure Fe, Mn, Al, Cr, and carbon powder. After being homogenized at 1250℃ for 12 h under a protective argon atmosphere, the ingots were hot-rolled to a final thickness of 6 mm. The plates obtained after hot rolling were subsequently solution heat-treated at 1200℃ for 2 h and then quenched rapidly into room-temperature water. The potentiodynamic polarization curves of the alloys were measured in 3.5% NaCl solution at 23℃ by using an EG&G Princeton Applied Research Model 273 galvanostat/potentiostat at a potential scan rate of 5 mVs^{-1}. The concentration of elements in the passive film formed on the surface of the alloys was examined by using a combined Auger electron spectroscopy (AES)/ X-ray photoelectron spectroscopy (XPS)/ secondary ion mass spectroscopy (SIMS) surface analysis system. The microstructures of the alloys were examined by optical microscopy and transmission electron microscopy (TEM). TEM

specimens were prepared by using a double-jet electropolisher with an electrolyte containing 15% perchloric acid, 25% acetic acid, and 60% ethanol. Electron microscopy was carried out using JEOL-2100 transmission electron microscope operating at 200 kV. Tensile tests were performed at room temperature using an Instron tensile testing machine at a strain rate of $5 \times 10^{-4} s^{-1}$. The specimens used for the tensile test were plates having a gauge length of 50 mm, width of 12 mm and thickness of 5 mm. The YS was measured at an offset strain of 0.2%, and the percent elongation was determined from the total elongation measured after fracture.

4-3 Results and discussion

Optical micrography examinations indicated that the as-quenched microstructure of alloys A (0Cr) through D (6Cr) was essentially γ phase with annealing twins. A typical example is shown in Figure 4.1a. The micrograph indicates that Cr could be completely dissolved within the γ matrix at 1200℃ for Cr $\leqq$ 6%. However, when the Cr content was increased up to 8%, some precipitates were observed to be formed on the grain boundaries, as illustrated in Figure 4.1b. TEM examinations indicated that the precipitates on the grain boundaries were $(Fe,Mn,Cr)_7C_3$ carbides ; these precipitates were similar to those observed by the present researchers in the as-quenched Fe-(7.1-9.1) wt.%Al -(29.2-30.2) wt.%Mn -(6.6-9.1) wt.%Cr-(0.94-1.07) wt.%C alloys [16,17]. TEM examinations also revealed that a high density of fine k′ carbides was present within the γ matrix in all the alloys. The fine k′ carbides having an L′1$_2$ (ordered f.c.c.) structure were formed by spinodal decomposition during quenching. An example is shown in Figures 4.1c and 1d. This result is similar to that obtained for the as-quenched Fe-9 wt.%Al-(28-30) wt.%Mn-(1.8-2) wt.%C alloys [20,21]. Accordingly, besides the presence of the coarse $(Fe,Mn,Cr)_7C_3$ carbides on the grain boundaries in alloy E (8Cr), the as-quenched microstructure of alloys
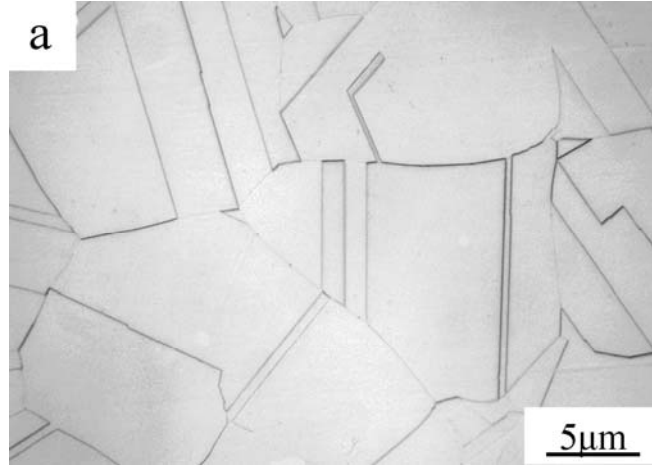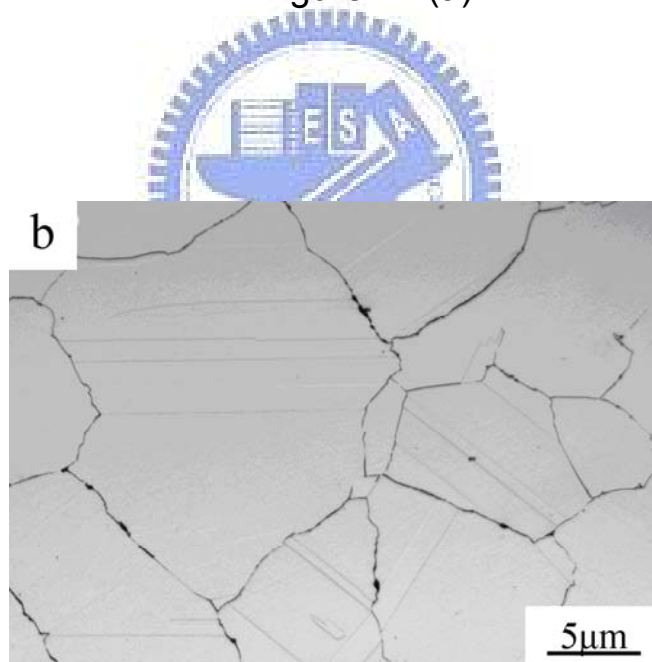
Figure 4.1(a)

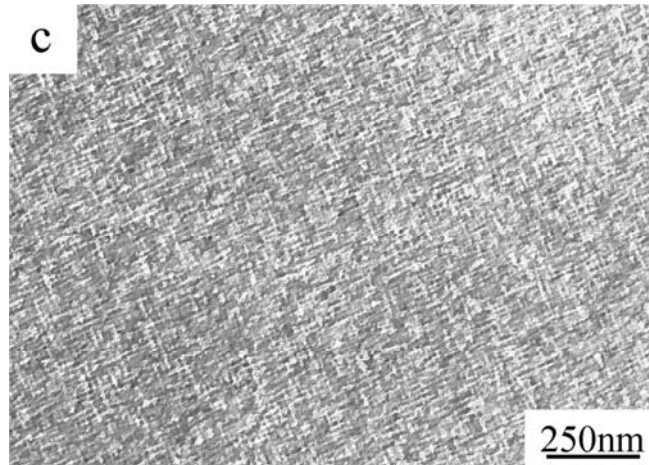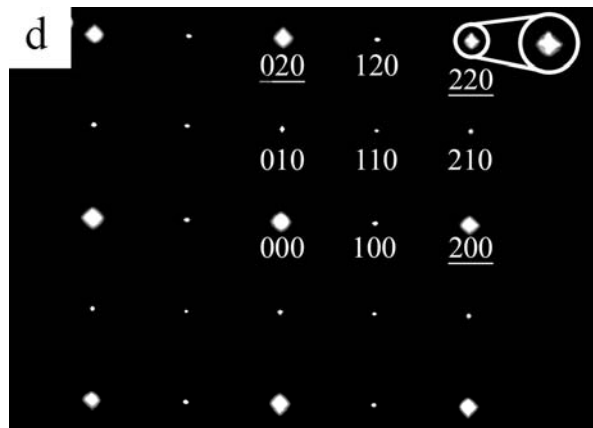
Figure 4.1(b)

Figure 4.1(c)

Figure 4.1(d)

Figure 4.1 Optical micrographs of present alloys: (a) alloy D (6Cr), and (b) alloy E (8Cr). Transmission electron micrographs of alloy D (6Cr): (c) $(100)_{k'}$ DF, and (d) a selected area diffraction pattern taken from a mixed region covering the γ matrix and fine k' carbides. The zone axis is [001] (hkl: γ matrix; hkl: k' carbide).

A (0Cr) through E (8Cr) was γ phase containing fine k′ carbides.

Figure 4.2 shows the potentiodynamic polarization curves of the five alloys measured in 3.5% NaCl solution. A broad passive region can be clearly observed in the curves of all the alloys except in the curve of the alloy not containing Cr. In addition, the width of the passive region increased as the Cr content increased from 3 to 6%, and the width decreased as the Cr content increased further up to 8%. The characteristic electrochemical parameters extracted from the polarization curves are listed in Table 4.1. As the Cr content changed, the corrosion potential (E_{corr}) of the alloys varied from -846 to -538 mV. Alloy D (6Cr) exhibited the noblest E_{corr} (-538 mV). Similarly, as the Cr content increased from 3 to 6%, the pitting potential (E_{pp}) drastically increased from -223 to -25 mV. However, when the Cr content was increased further up to 8%, E_{pp} became more negative (-412 mV). This indicated that alloy D (6Cr) had the highest resistivity to pitting damage. Figures 4.3a-d show the Auger depth profiles of the passive film formed on alloys A (0Cr), B (3Cr), D(6Cr), and E(8Cr), respectively. As can be clearly seen in these figures, broad peaks of Cr, Al, and O were observed at a depth of 0-2mm in alloys B(3Cr), D(6Cr), and E (8Cr) alloys. The presence of a layer of Cr and Al oxides in the passive film may play an important role in improving
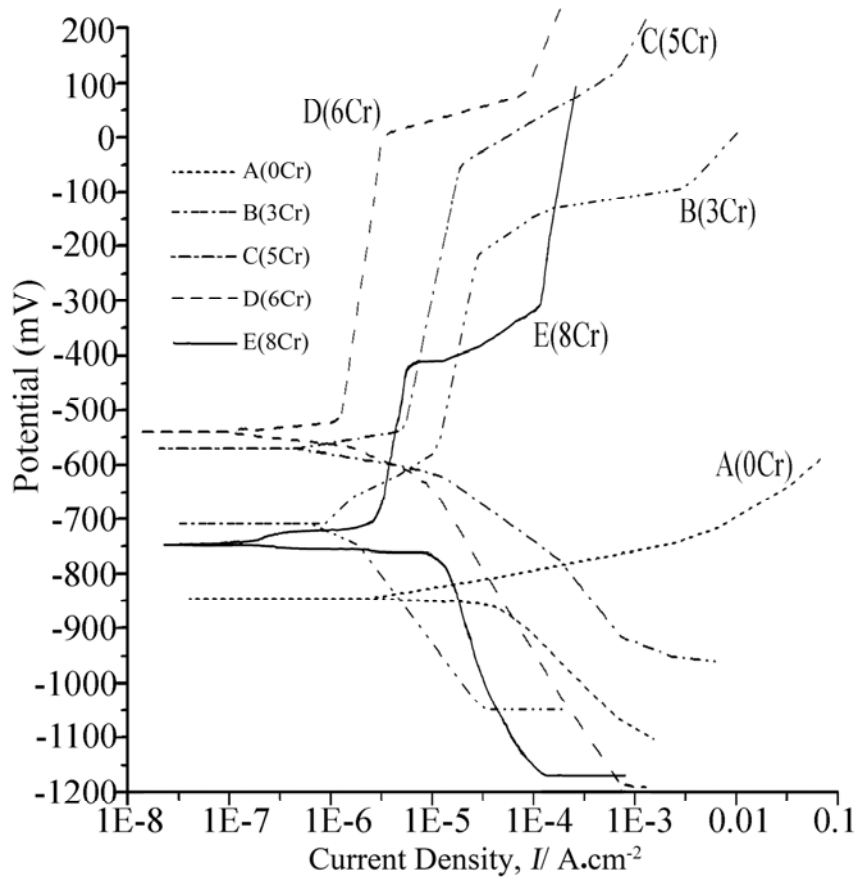
Figure 4.2 Potentiodynamic polarization curves for present five alloys
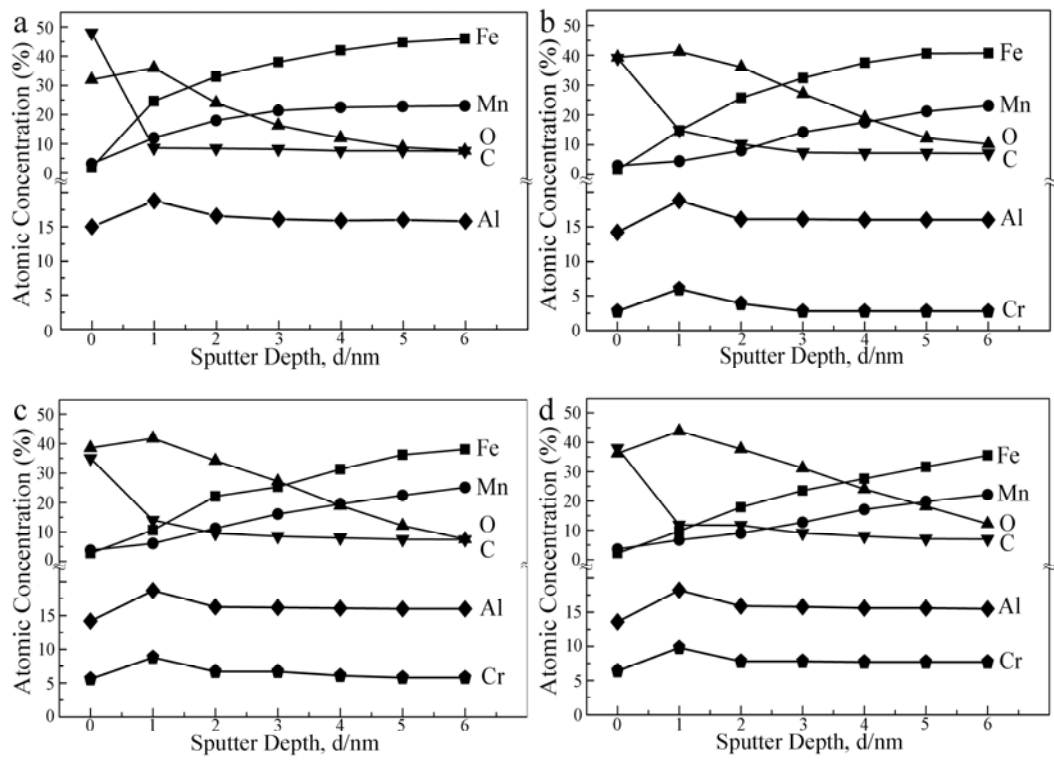
measured in 3.5% NaCl solution.

Figure 4.3 AES depth profiles of passive film of present alloys: (a) A (0Cr),

(b) B (3Cr), (c) D (6Cr), and (d) E (8Cr).

the corrosion resistance characteristics of alloys B (3Cr) through D (6Cr). However, the formation of the coarse Cr-rich $(Fe,Mn,Cr)_7C_3$ carbides resulted in a drastic decrease in the E_{corr} and E_{pp} values of alloy E (8Cr). As expected, the experimental results presented above were similar to those obtained for the as-quenched Fe-(7.1-9.1) wt.%Al-(29.2-30.2) wt.%Mn-(0-9.1) wt.%Cr-(0.94-1.07) wt.%C alloys [18, 19].

The tensile properties of the five as-quenched alloys investigated in the present study are also listed in Table 4.1. It can be clearly seen from the table that the UTS, YS, and elongation of alloy A (0Cr) were 1080 MPa, 868 MPa, and 55.5%, respectively. As the Cr content increased from 3 to 6%, the tensile strength slightly increased. Alloy D (6Cr) possessed the highest UTS (1122 MPa) and YS (902 MPa) with a good elongation of 36.5%. Owing to the high density of fine k′ carbides within the γ matrix, alloys A (0Cr) through D (6Cr) in the as-quenched condition could possess a remarkable combination of strength and ductility. This result is similar to that reported for the Fe -9 wt.%Al-28 wt.%Mn-1.8 wt.%C alloy [21]. However, when the Cr content was increased up to 8%, both the strength and elongation drastically reduced because of the formation of the coarse $(Fe,Mn,Cr)_7C_3$ carbides on the grain boundaries.

Table 4.1 Electrochemical parameters extracted from polarization curves

and mechanical properties of the present five alloys.

Alloy	Electrochemical parameters from polarization curves				Mechanical properties		
	E_{corr} (mV)	E_{cr} (mV)	E_{pp} (mV)	I_p (A·cm^{-2})	UTS (MPa)	YS (MPa)	El (%)
A (0Cr)	-846	—	—	—	1080	868	55.5
B (3Cr)	-710	-572	-223	1.5E-05	1092	876	47.2
C (5Cr)	-571	-524	-65	8.19E-06	1102	882	39.1
D (6Cr)	-538	-490	-25	9.12E-07	1122	902	36.5
E (8Cr)	-746	-652	-412	3.52E-06	984	835	22.6

E_{corr}, corrosion potential; E_{cr}, critical potential for active-passive transition; E_{pp}, pitting potential; I_p, passive current density, minimum value.
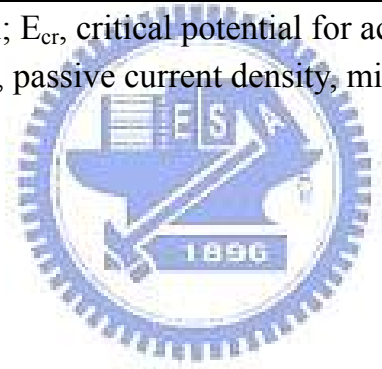
On the basis of the above observations, three important experimental results are obtained as discussed below. (I) A comparison of the results of this study with those of previous studies, revealed that the yield strength of alloy D (6Cr) was not only superior to that (410~550 MPa) of the as-quenched Fe-(7.8-10) wt.%Al -(28-34) wt.%Mn-(0-2.8) wt.%Cr-(0-1.75) wt.%M (M=Nb+V+Mo+W)-(0.85-1.3) wt.%C alloys but also comparable to that (665~1094 MPa) of the aged alloys [3-9, 11-15]. In addition, the E_{corr} and E_{pp} values of the alloys measured in 3.5% NaCl solution in previous studies were in the range of -920 to -789 mV and -500 to -240 mV, respectively [11-15]. Owing to the presence of a layer of Al and Cr oxides in the passive film, the E_{corr} and E_{pp} values of alloy D (6Cr) drastically increased to -538mv and -25mV, respectively. Therefore, it was concluded that the as-quenched alloy D (6Cr) possessed a better combination of high-strength, high-ductility, and moderate corrosion resistance. (II) The corrosion resistances of the present alloys in 3.5% NaCl solution were similar to those of the as-quenched Fe-(7.1-9.1) wt.%Al-(29.2-30.2) wt.%Mn-(3-9.1) wt.%Cr-(0.94-1.07) wt.%C alloys [16,17]. This implied that the presence of the fine k′ carbides within the γ matrix did not considerably affect the electrochemical behavior of the alloy in 3.5% NaCl solution. (III) The FeAlMnC alloy system was initially

developed with the intention of replacing the conventional FeNiCr stainless steels because of its high strength, good toughness, low density, and low cost. However, previous studies revealed that the FeAlMnC alloys exhibited poor corrosion resistance in aqueous environments

[11-15]. It is interesting to note that the characteristics of alloy D (6Cr) are similar to those of the conventional martensitic stainless steels, conventional martensitic stainless steels are commonly used for manufacturing components that require a combination of high strength and moderate corrosion resistance [22]. AISI 410 (12%Cr-0.10%C) is an example of martensitic stainless steels [22]. Therefore, in the following description, we will compare the properties of AISI 410 and alloy D (6Cr). The high strength and moderate corrosion resistance of the AISI 410 can be achieved by carrying out heat treatment, including austenitizing, air-quenching and tempering treatments [22]. After being tempered at a temperature between 250 and 593℃, the UTS, YS, and elongation were found to be 827~1337 MPa, 724~1089 MPa, and 20~17%, respectively [22]. Additionally, the E_{corr} and E_{pp} values of AISI 410 measured in 3.5% NaCl solution ranged from -675 to -312 mV and -250 to -100 mV, respectively [23-25]. The mechanical strength of alloy D (6Cr) was comparable to that of AISI 410, and alloy D exhibited better elongation

than AISI 410. In addition, the E_{pp} value (-25 mV) of alloy D (6Cr) was much higher than that (-250~-100 mV) of AISI 410. This might be attributed to the fact that although AISI 410 might have a Cr content of up to about 12%, a large amount of coarse Cr-rich $(Fe,Cr)_{23}C_6$ carbides precipitate within its martensitic matrix during tempering. The precipitation causes the Cr concentration, which is dependent on the Cr-rich carbides, to reduce considerably, and hence, the boundaries between the carbides and the martensitic matrix act as locations for nucleation and as anodic positions for pitting corrosion [26, 27]. Therefore, the pitting potential of the tempered AISI 410 decreases considerably. In contrast to the tempered AISI 410, there was no evidence of the formation of chromium carbides in the as-quenched alloy D (6Cr). Furthermore, the average particle size of the fine k′ carbides was only about 22 nm. In addition, the fine k′ carbide had the same crystal structure and a similar lattice parameter as the γ matrix, therefore, the interface between the k′ carbide and the γ matrix was completely coherent. Consequently, even at a considerably low Cr content, the pitting potential of alloy D (6Cr) was noticeably higher than that of the tempered AISI 410.

4-4 Conclusions

In this study, a new austenitic Fe-9 wt.%Al-28 wt.%Mn-6 wt.%Cr-1.8 wt.%C alloy is developed. The as-quenched alloy possesses a remarkable combination of high-strength, high-ductility, and moderate corrosion resistance, which is attributed to the presence of fine k′ carbides formed coherently within the γ matrix during quenching and to a layer of Cr and Al oxides in the passive film. The pitting potential E_{pp} (-25 mV) of alloy D (6Cr) measured in 3.5% NaCl solution is noticeably higher than that of the aged FeAlMnC alloys(-500~-240 mV) and the tempered AISI 410 martensitic stainless steel(-250~-100 mV). In addition, the tensile strength of alloy D is comparable to that of the aged FeAlMnC alloys and AISI 410.

References

1. C.N. Hwang, C.Y. Chao, T.F. Liu: Scripta Metall. 28 (1993) 263-268.

2. C.N. Hwang, T.F. Liu: Scripta Mater. 36 No.8 (1997) 853-859.

3. S.C. Tjong, S.M. Zhu: Mater. Trans. 38 No.2 (1997) 112-118.

4. I.S. Kalashnikov, O. Akselrad, M.S. Khadyev: Metal Sci. Heat Treat. 48 No.5-6 (2006) 219-225.

5. W.K. Choo, J.H. Kim, J.C. Yoon: Acta Mater. 45 No.12 (1997) 4877-4885.

6. I. Kalashnikov, O. Acselrad, A. Shalkevich, L.C. Pereira: J. Mater. Eng. Perform. 9 (2000) 597-602.

7. G.S. Krivonogov, M.F. Alekseyenko, G.G. Solov'yeva: Fiz. Metal. Metalloved. 39 No.4 (1975) 775-781.

8. I.S. Kalashnikov, O. Acselrad, A. Shalkevich, L.D. Chumakova, L.C. Pereira: J. Mater. Process Tech. 136 (2003) 72-79.

9. I.S. Kalashnikov, B.S. Ermakov, O. Akselrad, L.K. Pereira: Metal Sci. Heat Treat. 43 No.11-12 (2001) 493-496.

10. K.H. Han: Mater. Sci. Eng. A279 (2000) 1-9.

11. M. Ruscak, T.P. Perng: Corrosion Oct. (1995) 738-743.

12. W.T. Tsai, J.B. Duh, J.T. Lee: J. Mater. Sci. 22 (1987) 3517-3521.

13. J.B. Duh, W.T. Tsai, J.T. Lee: Corrosion Nov. (1988) 810-818.

14. S.C. Chang, J.Y. Liu, H.K. Juang: Corrosion 51 No.5 (1995) 399-406.

15. C.J. Wang, Y.C. Chang: Mater. Chem. Phys. 76 (2002) 151-161.

16. C.S. Wang, C.Y. Tsai, C.G. Chao, T.F. Liu: Mater. Trans. 48 (2007) 2973-2977.

17. Y. H. Tuan, C. S. Wang, C. Y. Tsai, C. G. Chao, T. F. Liu: Mater. Chem. Phys. 114 (2009) 595-598.

18. Y. H. Tuan, C. L. Lin, C. G. Chao, T. F. Liu: Mater. Trans. 49 No.7 (2008) 1589-1593.

19. C.F. Huang, K.L. Ou, C.S. Chen, C.H. Wang: J. Alloys Comp. 488 (2009) 246-249.

20. C.S. Wang, C.N. Hwang, C.G. Chao, T.F. Liu: Scripta Mater. 57 (2007) 809-812.

21. K.M. Chang, C.G. Chao, T.F. Liu: Scripta Mater. 63 (2010) 162-165.

22. J.R. Davis: *Stainless Steels*, (ASM International, OH, 1994), pp. 3-18.

23. U.M. Dawoud, S.F. Vanweele, Z. S-Smialowska: Corr. Sci. 33 No.2 (1992) 295-306.

24. N. Azzerri, F. Mancia, A. Tamba: Corr. Sci. 22 No.7 (1982) 675-687.

25. C.X. Li, T. Bell: Corr. Sci. 48 (2006) 2036-2049.

26. C.T. Kwok, H.C. Man, F.T. Cheng: Surface Coat. Tech. 126 (2000) 238-255.

27. C.T. Kwok, K.H. Lo, F.T. Cheng, H.C. Man: Surface Coat. Tech. 166 (2003) 221-230.

List of Publications

- **Journal Papers**

1. <u>GowDong Tsay</u>, ChunWei Su, YiHsuan Tuan, ChuenGuang Chao and TzengFeng Liu, "Phase separation from $L2_1$ to $(B2+L2_1)$ in Fe-24.6Al-7.5Ti alloy", published in Materials Transactions. Vol. 51(2010), No.10 pp.1934-1938

2. <u>GowDong Tsay</u>, ChihLung Lin, ChuenGuang Chao and TzengFeng Liu, "A New Austenitic FeMnAlCrC Alloy with High-Strength, High-Ductility, and Moderate Corrosion Resistance", published in Materials Transactions. Vol. 51(2010), No.12 pp.2318-2321

3. <u>GowDong Tsay</u>, YiHsuan Tuan, ChihLung Lin, ChuenGuang Chao, and TzengFeng Liu, "Effect of Carbon on Spinodal Decomposition in Fe-26Mn-20Al-C Alloys", accepted for publication in Materials Transactions. (2010,12)